Delft University of Technology

Document Version
Final published version

Licence
CC BY

Citation (APA)
Mohammadrezaei, S., Farajzadeh, R., & Niasar, V. (2026). Modeling the Drying Process of CO2-Water in Porous Media With a Novel Volume-of-Fluid Lattice Boltzmann Model. *Water Resources Research*, *62*(3), Article e2025WR040829. https://doi.org/10.1029/2025WR040829

Water Resources Research

RESEARCH ARTICLE
10.1029/2025WR040829

Modeling the Drying Process of CO_2-Water in Porous Media With a Novel Volume-of-Fluid Lattice Boltzmann Model

Saleh Mohammadrezaei[1], **Rouhi Farajzadeh**[2,3], **and Vahid Niasar**[1]

[1]Department of Chemical Engineering, University of Manchester, Manchester, UK, [2]Faculty of Civil Engineering and Geosciences, Delft University of Technology, Delft, The Netherlands, [3]Shell Global Solutions International B.V., The Hague, The Netherlands

Key Points:

- A new lattice Boltzmann model for modeling two-phase flow in porous media for high-contrast density and viscosity ratios was developed
- A lattice-Boltzmann model of coupled two-phase flow and evaporation was developed
- Pore-scale heterogeneity enhances the capillary-driven flow during evaporation

Supporting Information:

Supporting Information may be found in the online version of this article.

Correspondence to:

V. Niasar,
vahid.niasar@manchester.ac.uk

Citation:

Mohammadrezaei, S., Farajzadeh, R., & Niasar, V. (2026). Modeling the drying process of CO_2-water in porous media with a novel volume-of-fluid lattice Boltzmann model. *Water Resources Research*, *62*, e2025WR040829. https://doi.org/10.1029/2025WR040829

Received 23 APR 2025
Accepted 2 FEB 2026

Author Contributions:

Conceptualization: Rouhi Farajzadeh, Vahid Niasar
Data curation: Vahid Niasar
Formal analysis: Saleh Mohammadrezaei
Funding acquisition: Rouhi Farajzadeh, Vahid Niasar
Investigation: Saleh Mohammadrezaei, Vahid Niasar
Methodology: Saleh Mohammadrezaei, Vahid Niasar
Project administration: Vahid Niasar
Resources: Rouhi Farajzadeh, Vahid Niasar
Software: Saleh Mohammadrezaei
Supervision: Rouhi Farajzadeh, Vahid Niasar
Validation: Saleh Mohammadrezaei, Vahid Niasar
Visualization: Saleh Mohammadrezaei

Abstract Lattice Boltzmann (LB) modeling has been extensively applied to porous media processes, including evaporation. Former pore-scale LB models for evaporation rely on oversimplified assumptions, such as matched viscosities. However, in subsurface CO_2–brine systems, the viscosity ratio can exceed 100 under relevant temperature–pressure conditions. This study introduces a novel LB model based on the Volume-of-Fluid (VoF) method, capable of simulating two-phase flow in porous media with high-contrast viscosities and densities. The proposed VoF-LB model was further extended to model coupled evaporation and two-phase flow for water–CO_2 in porous media. The simulation results were validated against analytical benchmarks and a pore-scale micromodel experiment. The model was employed to explore how pore size distribution variability influences the drying front and the redistribution of water due to capillary suction, with implications for geological CO_2 storage in saline aquifers. This study presents two key advancements: (a) it demonstrates that the developed VoF-LB model accurately captures sharp phase interfaces and effectively handles extreme viscosity and density contrasts relevant to CO_2–water systems; (b) the validated VoF-LB model is applied to simulate drying in both 2D and 3D porous media, introducing a dimensionless parameter to quantify evaporation-driven mass transfer relative to capillary flow. The results reveal that pore-size heterogeneity and capillary-pressure gradients play a crucial role in shaping the drying interface and governing water redistribution. In 3D simulations, greater water-phase connectivity amplifies these effects compared to 2D, highlighting the significance of corner flow and extensive liquid connectivity—phenomena not fully captured in 2D.

1. Introduction

Drying in porous media is critical for a variety of applications. In agriculture, drying influences the soil moisture distribution, which directly affects crop yield and soil health (Or et al., 2013). In food and pharmaceutical industries, controlling the drying process is essential to maintain product quality, extend shelf life, and ensure stability (Prawiranto et al., 2019; Wheeler et al., 2024). In buildings, drying can cause salt precipitation, leading to structural damage and reduced durability (Godts et al., 2021; Qazi et al., 2019). However, the key motivation of our study is related to the geological carbon storage in saline aquifers, as one of the technological approaches to reduce the atmospheric CO_2 emission set by (IPCC, 2022). One of the operational challenges faced in the real-world application of geological CO_2 storage is that during the injection of dry CO_2 into saline aquifers, evaporation of water in rocks is triggered and salt aggregates form, which can potentially cause permeability loss and pressure build-up (Ott et al., 2015; Page et al., 2020; Peysson et al., 2014; Pruess & Müller, 2009). A key aspect of this interaction is the evaporation triggered by the contact between CO_2 and brine, driven by the difference in water vapor pressure. This not only alters the salinity but, also impacts the porosity and permeability of the storage formation due to salt precipitation in the rock pores (Ott et al., 2015; Peysson et al., 2014; Pruess & Müller, 2009).

For the process of drying from the surface of a porous medium, previous studies have shown that evaporation occurs in two distinct stages (Lehmann et al., 2008). Initially, the evaporation rate is high and remains so as long as water within the porous medium retains connectivity to the surface. However, once this connectivity is lost, the evaporation rate decreases significantly, marking the beginning of the second stage of drying. Numerous experimental studies have corroborated these observations (Or et al., 2013). These findings suggest that capillarity plays a pivotal role in redistributing water, functioning as a "pumping" mechanism during the drying process. In contrast, the drying process during CO_2 injection into saline aquifers exhibits a key difference: advective forces first displace water, followed by evaporation occurring behind the two-phase front (Ott

Writing – original draft:
Saleh Mohammadrezaei
Writing – review & editing:
Saleh Mohammadrezaei, Vahid Niasar

et al., 2014). Previous studies have also demonstrated the capillary pumping effect, often referred to as capillary-driven backflow (Ott et al., 2021). One of the key questions in the drying process in CO_2-brine-rock system is how the interplay of evaporation and pore-scale capillary forces control the morphology and evolution of the drying front, particularly under CO_2-water viscosity and density contrasts. Addressing this question is crucial because an increase in capillary-driven water redistribution ("capillary pumping") can accelerate local salt precipitation and, over time, damage reservoir porosity and permeability.

Experimental and field-scale observations show that water redistribution and drying-front evolution in CO_2-injected saline aquifers can lead to local salt precipitation, reducing porosity and injectivity (Baumann et al., 2014; Bette & Heinemann, 1989; Jasinski et al., 1997). Predicting this behavior requires a model that captures how fluid interfaces move, reconnect, and break within the intricate pore geometry of rocks. Traditional continuum or Darcy-scale models, which treat the pore space as a homogenised continuum, cannot easily describe thin water films, corner flow, and other pore-scale connectivity mechanisms essential for CCS application. A pore-scale approach is therefore necessary to resolve these interfaces accurately and to capture how capillarity, evaporative mass transfer, and potential viscous effects compete.

Pore-scale simulations provide a detailed understanding of multiphase flow and transport in porous materials using various method such as dynamic pore-network modeling (Joekar-Niasar & Hassanizadeh, 2012), lattice Boltzmann modeling (Liu et al., 2016). The LBM is particularly effective in modeling details of the flow and transport within the complex pore morphology. LBM's versatility in adapting to various interface conditions, that is fluid-fluid and solid-fluid interfaces between two fluids, as well as capturing the wettability effects on liquid-solid surfaces (An et al., 2022; Timm et al., 2016), enhances its applicability. Additionally, its notable accuracy, combined with a higher computational speed and the simplicity of its discrete equations have made LBM an attractive and widely adopted method in the field (An et al., 2021; Sukop & Or, 2004).

Nevertheless, the basic form of the Lattice Boltzmann Equation (LBE) does not inherently consider the interactions between two phases. Therefore, modifications to the LBE are necessary to incorporate inter-particle forces in multiphase flow systems. Over the years, various models have been proposed for simulating multiphase flow using the LBM. These include the Color Model by Gunstensen et al. (1991), which assigns different "colors" to fluids for interface tracking, and the Pseudo-Potential Model by Shan and Chen (1993); Shan and Chen (1994), which introduces pseudo-potential forces for particle interactions. Additionally, the Free Energy Model by Swift et al. (1995, 1996) aims for thermodynamic consistency, and the Phase-Field Model (Alpak et al., 2018; Frank et al., 2018; Kim & Lowengrub, 2005) handles complex interfacial dynamics through a continuous transition zone marked by a phase field variable. The previously introduced multiphase LB models would not meet the specific materials' physical properties needed in this study. Pseudo-potential and free energy models offer valuable frameworks for simulating multiphase systems across a range of density ratios. However, their diffuse interface formulation may present challenges in capturing the sharp fluid-fluid interfaces and intricate interfacial dynamics necessary for accurately modeling the capillary and evaporative interactions involved in CO_2 injection in porous media. While both sharp and diffuse interface approaches can be effective, it is critical that the interface thickness-whether explicitly sharp or computationally diffuse-remains much smaller than the characteristic pore sizes to ensure accurate representation in porous media applications.

Zachariah et al. (2019) used a 2D pseudo-potential model for simulating invasion patterns in porous media during the drying process. Sourya et al. (2023) studied the drying of porous materials in the capillary regime using Shan-Chen LBM. They demonstrated the effects of convection-diffusion boundary conditions and the differences between diffusion-dominated and convection-diffusion kinetics. Panda et al. (2020) used the Shan Chen LBM to simulate a bundle of four capillaries, revealing the micro-scale dynamics such as capillary pumping, film formation, and vapor transport. Fei et al. (2022) employed a multiphase and multi-component LBM to examine the convective drying phenomena in porous materials. Furthermore, their subsequent investigation explored the impact of modifying the initial vapor concentration and the surface contact angle on the rates of evaporation (Fei et al., 2023). However, these models have limitations in their representation of the physical characteristics of the fluid like viscosity and density and the detailed geometrical intricacies of the porous medium.

Existing pore-scale LB models for simulating drying processes during CO_2 injection exhibit limitations due to their oversimplified assumptions and dimensional constraints. The aforementioned models assume a viscosity ratio of 1 (Fei et al., 2022; Panda et al., 2020; Sourya et al., 2023; Zachariah et al., 2019), which cannot represent the physical CO_2-brine viscosity ratio which can vary from 10 to over 100, depending on the temperature and pressure conditions (Georgiadis et al., 2010). Furthermore, the previous LB models for the drying process were performed in two-dimensions, while it is known that the two dimensionality has a major impact on percolation pathways, film continuity and interfacial phenomena for the two immiscible fluids compared to the complex three-dimensional porous media. Fluid-fluid interfaces control the evaporation and precipitation during CO_2 injection and the pore-scale model must be capable of capturing the interfaces based on the physical properties of rock-brine-CO_2. Moreover, for simulating the complex porous media of subsurface rock, particularly at micro scale, the model should have the capability to resolve intricate details within micrometer-scale sizes.

This paper contributes to the fundamental science of two-phase flow in porous media in two key areas: (a) To our knowledge, there is no porous-media LB model that robustly handles large density and viscosity contrasts (as in CO_2-water systems, which can be over 100) while preserving sharp-interface dynamics in complex pore geometries and accounting for interfacial mass transfer (evaporation). To address this, we develop a volume-of-fluid (VOF) lattice Boltzmann model that simulates coupled two-phase flow and evaporation in porous media at high density and viscosity ratios, while maintaining sharp liquid–gas interfaces. (b) Drying of water in contact with CO_2 is simulated at pore scale, where capillary force and mass exchange due to evaporation govern water redistribution and front movement. The dynamics of water redistribution in 2D and 3D domains are investigated to identify conditions under which capillary pumping significantly accelerates salt precipitation.

2. Materials and Methods

We begin by outlining our numerical methodology, which is based on a LB framework for capturing multiphase flow and evaporation dynamics in porous media. To analyze the evolution of the drying front and water redistribution, we introduce a dimensionless parameter, which quantifies the relative influence of evaporation and capillarity on mass redistribution. By characterizing the balance between these fluxes, this parameter serves as a key metric for designing case studies that explore the complex drying dynamics in porous systems, including the effects of heterogeneity and geometry. Following this analysis, we detail the numerical domains, boundary conditions, and initial conditions of the LB model.

2.1. LB Method for Coupled Two-Phase Flow-Evaporation in Porous Media

2.1.1. Principles of the LB Method

The Boltzmann equation was established to describe the kinetic theory of gases based on statistical mechanics (Boltzmann, 1964). This equation governs the evolution of the particle distribution function f over time:

$$\frac{Df}{Dt} = \frac{\partial f}{\partial t} + \boldsymbol{\zeta} \cdot \nabla f + \mathbf{F} \cdot \nabla_{\mathbf{p}} f = \boldsymbol{\Omega}(\mathbf{f}), \tag{1}$$

where $f = f(\mathbf{x}, \boldsymbol{\zeta}, t)$ is the single-particle distribution function, $\mathbf{x}$ represents position, $\boldsymbol{\zeta}$ is the microscopic velocity, t denotes time, and $\mathbf{F}$ signifies external forces. Here, $\boldsymbol{\Omega}(\mathbf{f})$ represents the collision operator, which accounts for the effect of particle collisions on the distribution function.

The Multiple-Relaxation-Time (MRT) model in the LBM offers enhanced stability and precision by employing various relaxation times for different moments of the distribution functions, especially useful in complex flow simulations on the D3Q19 lattice (3 dimensions, 19 discrete velocities). The MRT collision operator is expressed as follows:

$$\boldsymbol{\Omega}(\mathbf{f}) = -\mathbf{M}^{-1} \cdot \mathbf{S}(\mathbf{m} - \mathbf{m}^{\mathrm{eq}}), \tag{2}$$

where $\mathbf{f}$ is the vector of distribution functions, $\mathbf{m}$ and $\mathbf{m}^{\mathrm{eq}}$ denote the vectors of moments and equilibrium moments, respectively. The transformation matrix $\mathbf{M}$ maps the distribution function to moment space, and $\mathbf{S}$ is a diagonal matrix of relaxation times (De Rosis & Coreixas, 2020).

In the LBM, the equilibrium distribution function $\mathbf{f}^{\mathrm{eq}}$ is typically derived from the Maxwell-Boltzmann distribution, approximated for use in discrete lattice systems as follows:

$$f_i^{\mathrm{eq}} = w_i \rho \left(1 + \frac{\mathbf{c}_i \cdot \mathbf{u}}{c_s^2} + \frac{(\mathbf{c}_i \cdot \mathbf{u})^2}{2c_s^4} - \frac{|\mathbf{u}|^2}{2c_s^2} \right), \tag{3}$$

where f_i^{eq} is the equilibrium distribution for the i-th direction, ρ represents the fluid density, w_i are weights for each lattice direction, $\mathbf{c}_i$ are discrete velocities, and $\mathbf{u}$ is the macroscopic velocity of the fluid with c_s as the lattice speed of sound. At each time step, we evaluate $f_i^{\mathrm{eq}}(\rho, \mathbf{u})$ from Equation 3 and form the equilibrium moments $m^{\mathrm{eq}} = \mathbf{M}\,\mathbf{f}^{\mathrm{eq}}$ used in the MRT collision of Equation 2. The post-collision moments are $m^{\mathrm{post}} = m - \mathbf{S}(m - m^{\mathrm{eq}})$, followed by $\mathbf{f}^{\mathrm{post}} = \mathbf{M}^{-1} m^{\mathrm{post}}$.

For a D3Q19 lattice, the weights w_i and discrete velocities $\mathbf{c}_i$ are given by:

$$w_i = \begin{cases} \frac{1}{3} & \text{for } i = 0, \\ \frac{1}{18} & \text{for } i = 1, \ldots, 6, \\ \frac{1}{36} & \text{for } i = 7, \ldots, 18, \end{cases} \tag{4}$$

$$\mathbf{c}_i = \begin{cases} (0,0,0) & \text{for } i = 0, \\ (\pm 1,0,0), (0, \pm 1, 0), (0,0, \pm 1) & \text{for } i = 1, \ldots, 6, \\ (\pm 1, \pm 1, 0), (\pm 1, 0, \pm 1), (0, \pm 1, \pm 1) & \text{for } i = 7, \ldots, 18. \end{cases} \tag{5}$$

The fluid viscosity ν in the LBM is related to the relaxation time τ and the lattice speed of sound c_s as follows:

$$\nu = c_s^2 \left(\tau - \frac{1}{2} \right), \tau > 0.5 \tag{6}$$

to assure positive viscosity. Using the distribution functions, the macroscopic density and velocity at each lattice site are determined by:

$$\rho = \sum_i f_i, \tag{7}$$

$$\rho \mathbf{u} = \sum_i \mathbf{c}_i f_i. \tag{8}$$

2.1.2. VOF-Based LB Method

Thürey et al. (2005) developed the foundation of the VOF-based LBM. This method has been mostly used in modeling free surface flow (Körner et al., 2005; Mohammadrezaei et al., 2022; Thorimbert et al., 2019). In this study, we further extended the VOF-based LBM model (Mohammadrezaei et al., 2022) implemented in the open-source Palabos (Latt et al., 2021) library by incorporation of coupled drying process. This enables the modeling of two-phase flow and evaporation in porous media for CO_2-brine fluids with their viscosities and densities.

The VOF-LBM classifies cells within the simulation domain as “empty”, which can fill up with fluid as the simulation progresses. The core of this methodology is the concept of “interface cells”, which form a transitional boundary between fluid-filled and empty regions. The simulation focuses on three primary processes at these interface cells: the computation of interface movement, the application of boundary conditions at the fluid interface, and the periodic re-initialization of cell types to reflect the fluid's dynamic nature.

The VOF-LBM introduces a secondary lattice, encompassing the distribution functions of a second fluid, allowing for a refined representation of fluid interactions, particularly at boundaries. This method can handle high contrasts in density and viscosity of fluids while maintaining a distinct, sharp interfaces. Figure 1 shows an overview of these steps that explain the function of interface cells in the VOF-LBM simulation framework.

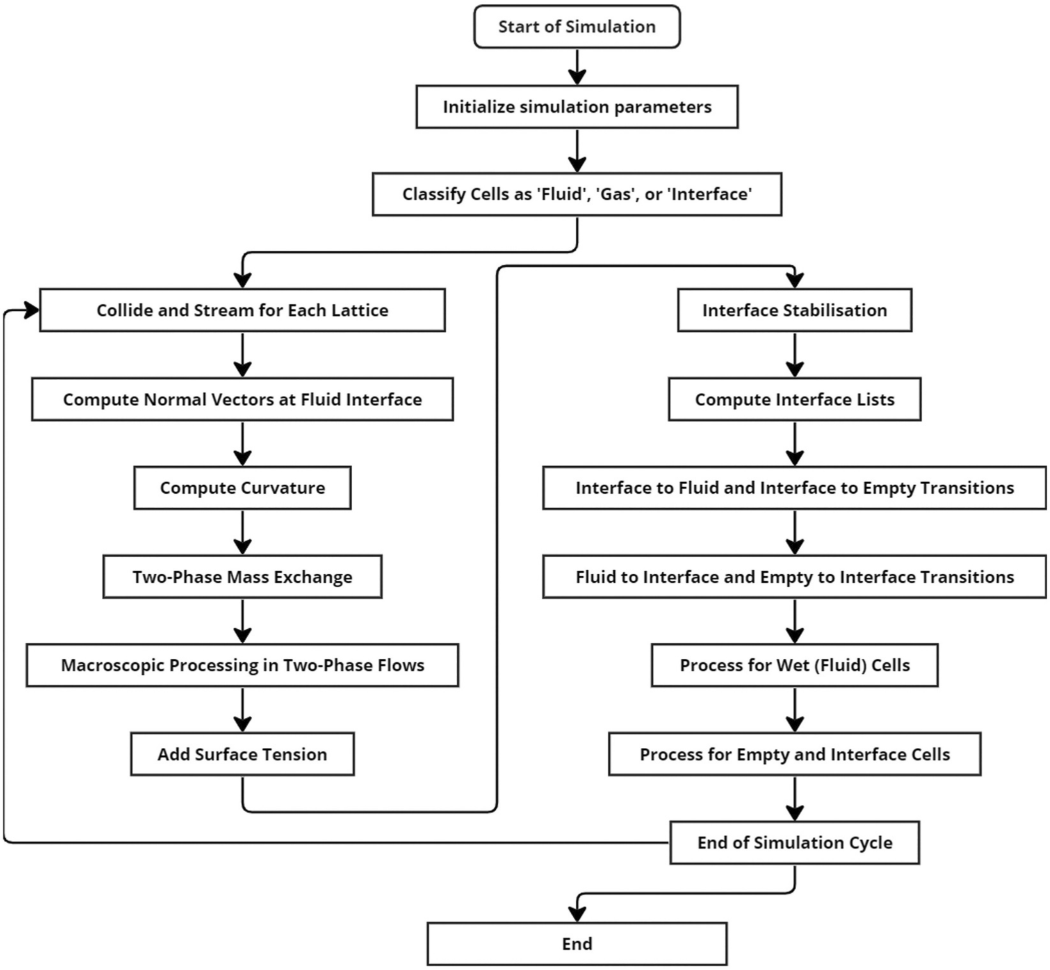

Figure 1. Overview of simulation procedures illustrating the role of interface cells in the VOF-based Lattice Boltzmann framework.

Each cell in the computational domain is categorized based on a volume fraction, ϵ, which is defined as the ratio of cell mass m to the density ρ of the fluid phase:

$$\epsilon = \frac{m}{\rho}. \tag{9}$$

Based on the value of ϵ, cells are assigned as follows: fluid cells ($\epsilon = 1$), gas cells ($\epsilon = 0$), and interface cells ($0 < \epsilon < 1$). Interface cells form a transitional layer that delineates fluid-filled and empty cells, facilitating the simulation of complex fluid dynamics near the interface. Figure 2 provides an overview of the processes that govern the evolution of interface cells in the VOF-LBM framework.

The VOF-based LBM operates on two primary lattices corresponding to gas and fluid phases, with collision and streaming steps applied independently to each. The interaction between these lattices occurs specifically at interface cells, where additional interface tracking and mass exchange mechanisms are employed to capture phase transitions and surface dynamics.

The collision and streaming steps within LBM evolve the distribution functions independently for each phase before interactions are computed at the interface. These steps maintain local fluid momentum and mass conservation within each lattice while enabling interaction at boundaries where the phases meet.

The interface cells are processed to account for curvature and surface tension, which are essential for accurately capturing capillary forces at the fluid-fluid boundary. For surface tension modeling, the normal vector **n** at the

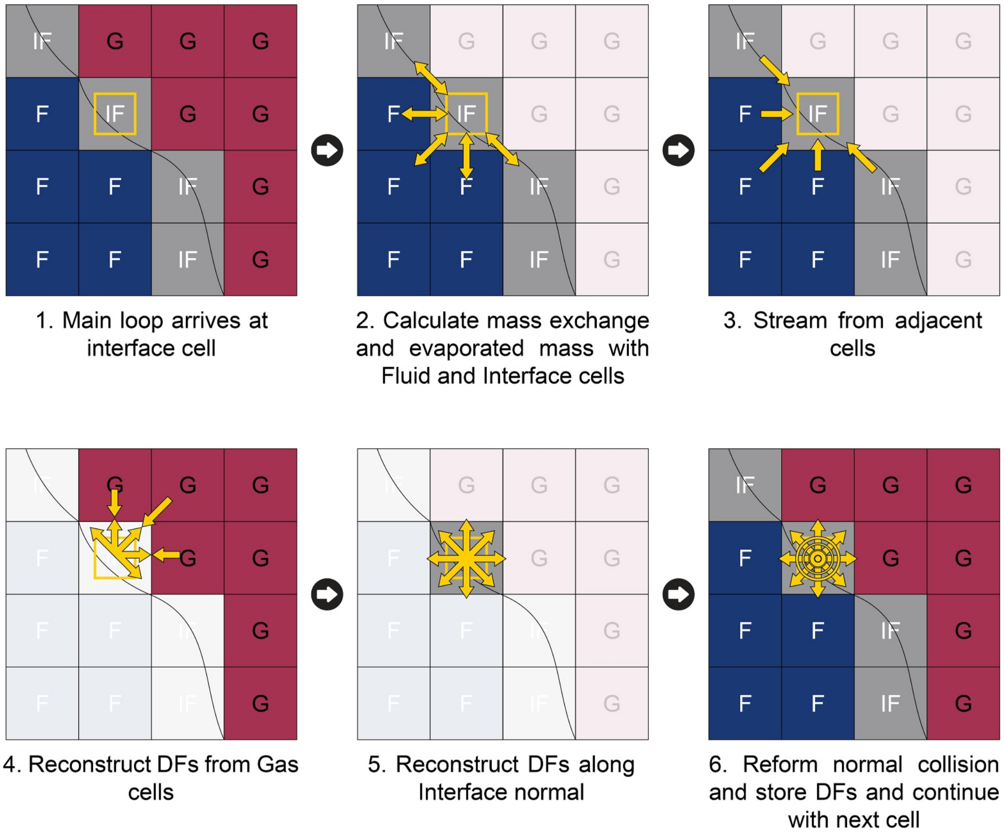

Figure 2. Summary of the processes that must be completed for a sample interface cell. Symbols G, F and IF stand for gas, liquid and interface cells, respectively. Here, DF stands for distribution function.

interface is computed using the contact angle θ_{eq}, which influences how the fluid interface aligns near solid boundaries:

$$\mathbf{n} = \cos(\theta_{\text{eq}}) \cdot \mathbf{n}_{\text{wall}} + \sin(\theta_{\text{eq}}) \cdot \mathbf{n}_{\text{tangent}}. \tag{10}$$

Here, $\mathbf{n}_{\text{wall}}$ and $\mathbf{n}_{\text{tangent}}$ are unit vectors normal and tangent to the solid surface, respectively. The divergence of this adjusted normal vector field is used to determine the mean curvature κ at each interface cell:

$$\kappa = \nabla \cdot \mathbf{n}. \tag{11}$$

The pressure difference across the interface due to surface tension is then calculated as:

$$\Delta P = 2\sigma\kappa + \left(\mu_d \frac{\partial \mathbf{u}_d}{\partial \mathbf{n}} - \mu_c \frac{\partial \mathbf{u}_c}{\partial \mathbf{n}}\right), \tag{12}$$

where σ is the surface tension, and μ_c and μ_d are the dynamic viscosities of the continuous and dispersed phases, respectively. Here $U_c = \mathbf{u}_c \cdot \mathbf{n}$ and $U_d = \mathbf{u}_d \cdot \mathbf{n}$ denote the normal velocity components at the interface on the continuous (c) and dispersed (d) sides, and $\partial/\partial\mathbf{n} \equiv \mathbf{n} \cdot \nabla$ denotes differentiation along the unit normal $\mathbf{n}$ oriented from c to d. This expression accounts for the capillary pressure and the viscous normal-stress jump across the interface, ensuring a consistent interfacial force balance.

To refine the physical accuracy of the two-phase flow simulation, macroscopic quantities such as density ρ, momentum $\mathbf{j}$, and volume fraction ϵ are periodically adjusted at interface cells. Small discrepancies that arise due to numerical errors are corrected by redistributing mass, which preserves mass conservation and flow accuracy across interfaces. The density and momentum adjustments are computed as:

$$\rho_{\text{new}} = \frac{m_{\text{cell}}}{V_{\text{cell}}}, \quad \mathbf{j}_{\text{new}} = \rho_{\text{new}} \cdot \mathbf{u}_{\text{avg}}. \tag{13}$$

Here $V_{\text{cell}} = \Delta x^3$, $m_{\text{cell}} = \sum_i f_i$, and $\mathbf{u}_{\text{avg}} = \mathbf{j}/\max\left(m_{\text{cell}},\ \rho_{\min} V_{\text{cell}}\right)$ with $\mathbf{j} = \sum_i \mathbf{c}_i f_i$ (cf. Equations 7 and 8); in practice we overwrite only the conserved MRT moments (density, momentum) to match $\left(\rho_{\text{new}}, \mathbf{j}_{\text{new}}\right)$, leaving higher-order moments unchanged. These corrections ensure that fluid properties such as density and momentum remain consistent, improving the model's stability and accuracy in capturing the effects of external forces, including gravitational forces.

Cell states are dynamically managed based on volume fraction ϵ, stabilizing the interface by reassigning cell types as liquid, gas, or interface. Transition criteria are defined to prevent abrupt state changes, based on a stabilizing threshold $\alpha = 1 \times 10^{-3}$:

$$\epsilon = \begin{cases} \text{liquid state}, & \text{if } \epsilon > 1 - \alpha, \\ \text{gas state}, & \text{if } \epsilon < \alpha, \\ \text{interface state}, & \text{if } \alpha \leq \epsilon \leq 1 - \alpha. \end{cases} \tag{14}$$

By ensuring smooth transitions between states, this approach maintains interface stability, preventing unrealistic phase changes.

To accurately reflect the impact of external forces, momentum updates are applied to all cell types, including interface cells. For liquid cells, momentum is updated according to:

$$\mathbf{J}_{\text{new}} = \mathbf{J} + \rho_{\text{default}} \cdot \tau \cdot \mathbf{F}, \tag{15}$$

where τ is the relaxation time, and $\mathbf{F}$ represents external forces. This update ensures that external influences such as gravity are accurately represented within the fluid dynamics, contributing to the realistic simulation of multiphase interactions across the domain.

We extend the two-lattice free-surface LBM to incorporate evaporation at the liquid–gas interface. Evaporation is restricted to interface cells identified by the volume fraction ϵ defined earlier. Consistent with the transition criterion using the stabilizing threshold α, we define an indicator

$$\chi_\Gamma(\mathbf{x}) = \begin{cases} 1, & \alpha \leq \epsilon(\mathbf{x}) \leq 1 + \alpha, \\ 0, & \text{otherwise}, \end{cases} \tag{16}$$

so that sources act only where a liquid–gas interface is present.

For each phase $(\cdot) \in \{\ell, g\}$, the evolution includes collision, streaming, standard forcing and an evaporation source:

$$f_i^{(\cdot)}(\mathbf{x} + \mathbf{c}_i \Delta t, t + \Delta t) = f_i^{(\cdot)}(\mathbf{x}, t) - \left[\mathbf{M}^{-1}\mathbf{S}\right]_{ij} \left(m_j^{(\cdot)} - m_j^{(\cdot),eq}\right) + F_i^{(\cdot)} + S_i^{(\cdot),\text{evap}}. \tag{17}$$

The evaporation sources are formulated to conserve both mass and momentum. The mass removed from the liquid is exactly added to the gas, and the transferred mass carries a single interfacial velocity $\mathbf{u}_I$ to avoid spurious recoil. The moment constraints are

$$\sum_i S_i^{\ell,\text{evap}} = -\chi_\Gamma\ \dot{m}\ \Delta t, \qquad \sum_i \mathbf{c}_i S_i^{\ell,\text{evap}} = -\chi_\Gamma\ \dot{m}\ \mathbf{u}_I\ \Delta t, \tag{18}$$

$$\sum_i S_i^{g,\text{evap}} = +\chi_\Gamma\ \dot{m}\ \Delta t, \qquad \sum_i \mathbf{c}_i S_i^{g,\text{evap}} = +\chi_\Gamma\ \dot{m}\ \mathbf{u}_I\ \Delta t, \tag{19}$$

where $\dot{m}$ is the total mass transfer rate per interface cell. In this work, we set $\mathbf{u}_I = \mathbf{u}_\ell$, that is the liquid velocity at the interface, which is consistent with evaporation where mass leaves the liquid carrying its local momentum.

Applying a Chapman–Enskog expansion to the above system (see Appendix A) with the source treated as $O(\epsilon)$ recovers, for the liquid phase,

$$\frac{\partial \rho_\ell}{\partial t} + \nabla \cdot (\rho_\ell \mathbf{u}_\ell) = -\chi_\Gamma\ \dot{m}, \tag{20}$$

$$\frac{\partial(\rho_\ell \mathbf{u}_\ell)}{\partial t} + \nabla \cdot (\rho_\ell \mathbf{u}_\ell \mathbf{u}_\ell) = -\nabla p_\ell + \nabla \cdot \left[\nu_\ell \rho_\ell \left(\nabla \mathbf{u}_\ell + \nabla \mathbf{u}_\ell^{\mathrm{T}}\right)\right] + \rho_\ell\, \mathbf{F}, \tag{21}$$

with $p_\ell = c_s^2 \rho_\ell$ and ν_ℓ given by Equation 6. The gas-phase equations are analogous with the opposite sign in the continuity source. Because the same $\mathbf{u}_I$ is used in both phases, no recoil term appears and total momentum is conserved.

The evaporation rate is proportional to the local interfacial area represented in the cell. Denoting this area by A_{int}, the per-cell transfer rate is

$$\dot{m} = \dot{m}''\ A_{\mathrm{int}}, \tag{22}$$

where $\dot{m}''$ is the evaporation mass flux per unit area. In this study, consistent with a near-well, dry CO_2 environment, we assume an isothermal, well-mixed gas with negligible water vapor so that $\dot{m}''$ is constant in space and time. To maintain the constant-pressure reservoir assumption, open boundary conditions are imposed so that the added gas-phase mass is advected out of the domain, preventing pressure drift.

This evaporation model conserves mass and momentum, reproduces the expected macroscopic balances, and remains consistent with the pore-scale isothermal conditions considered here.

2.2. Analysis of Water Redistribution Due To Drying in Porous Media

In this section, we identify the main factors that shape the drying front evolution and water redistribution in porous media, providing a foundation for systematically defining our case studies. Understanding these factors is crucial, as they determine how evaporation, capillary forces, and inherent heterogeneities interact to drive drying behavior.

Previous studies, notably the work of Lehmann and Or (2009), demonstrated that in a vertically heterogeneous system composed of fine and coarse domains, evaporation is primarily sustained by capillary-driven liquid flow from the coarse domain to the fine-textured surface. They identified two key characteristic lengths governing this process: (a) the air-entry characteristic length, which defines the depth at which air invades the fine-textured domain, and (b) the evaporative characteristic length, which describes the extent of liquid connectivity sustaining high evaporation rates before transitioning to a diffusion-controlled regime. Their macroscopic model provided a fundamental framework for understanding capillary coupling but lacked a pore-scale representation of the underlying fluxes.

We refine this perspective by introducing a pore-scale mass balance formulation that explicitly accounts for the impact of pore-size heterogeneity on capillary-induced water redistribution. This approach is particularly relevant to our VOF-LBM simulations to define our numerical domains. Figure 3 provides a schematic view of two systems at (a) pore scale, and (b) Darcy scale. Figure 3a shows two inter-connected capillary tubes with two different radii and Figure 3b shows two inter-connected porous media with different pore-size distributions.

The mass balance for a group of pores in fine and coarse domains of Figure 3b can be written as:

$$\frac{dh_i(t)}{dt} = -\frac{\mathcal{J}}{\rho} \pm \frac{Q_{ij}(t)}{\mathcal{A}_{ij}}, \tag{23}$$

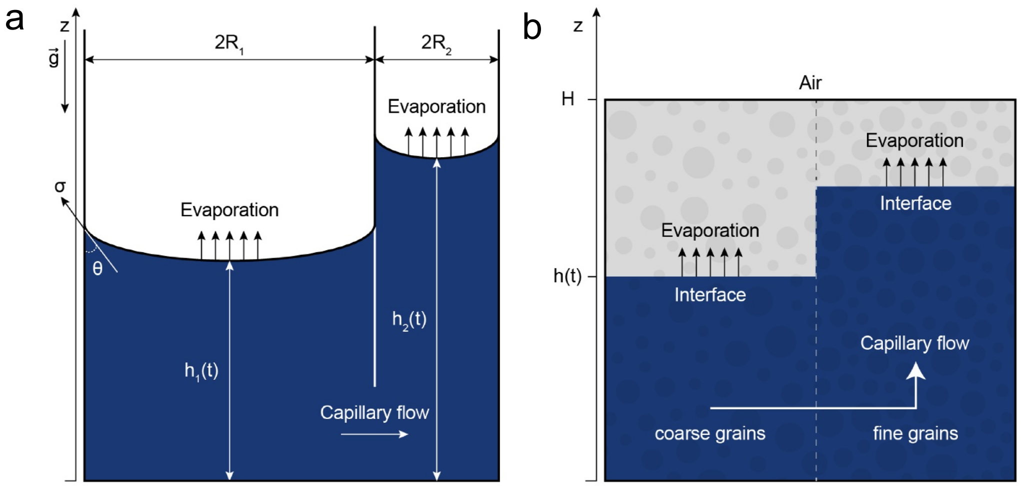

Figure 3. Schematic representation of (a) two interconnected vertical capillary tubes, and (b) two-layered porous medium.

where $h_i(t)$ is the liquid height in the domain i, $\mathcal{J}$ is the evaporation flux (kg m^{-2} s^{-1}), ρ is the liquid density, $\mathcal{A}_{ij}$ is interface area between the two domains i and j, and $Q_{ij}(t)$ is the capillary-induced water flux between the domains i and j.

During drying of porous media, the evaporation process typically transitions through three stages: the constant rate period (CRP), the receding front period (RFP), and the falling rate period (FRP) (Chauvet et al., 2009). The principal driver of these transitions is the difference in water vapor pressure (or chemical potential) between the liquid phase in the pores and the external gas phase.

In our simulations, we assumed that the evaporation flux $\mathcal{J}$ is constant. This assumption simplifies both the analytical derivation and the numerical method, since otherwise we would need to also model vapor transport in the gas phase.

At the pore scale (Figure 3a), the mass flux between the two domains can be explained by the Hagen-Poiseuille equation $Q_{ij}(t) = -\mathcal{K}_{ij}\mathcal{A}_{ij}\nabla p_{ij}$, in which $\mathcal{K}_{ij}$ is proportional to $r_{p_{ij}}^2/\mu$. Since water flux is induced by capillarity and pressure drop is neglected in the gas phase we can write $\nabla p_{ij} = -\nabla p_{ij}^c$. At pore scale the p^c can be approximated by Young-Laplace equation:

$$p^c \approx \frac{\sigma \cos \theta}{r_p} \tag{24}$$

in which r_p is the characteristic pore size. Thus, we can approximate $Q_{ij}(t) = -\frac{\sigma \cos \theta}{\mu}\mathcal{A}_{ij}\nabla r_{p_{ij}}$,

Equation 23 can be rephrased as

$$\frac{dh_i(t)}{dt} \approx -\frac{\mathcal{J}}{\rho} \mp \frac{\sigma \cos \theta}{\mu}\frac{\Delta r_{p_{ij}}}{\mathcal{L}_{ij}}, \tag{25}$$

Here $\mathcal{L}_{ij}$ is characteristic distance over which r_p changes. This equation demonstrates that the gradient of pore size distribution at the heterogeneity interface leads to the imbalance of capillary forces in two domains and thus capillary-induced flow. Based on that we introduce a dimensionless number Γ:

$$\Gamma_{ij} = \frac{\mathcal{J}}{\rho}\left(\frac{\sigma \cos \theta \Delta r_{p_{ij}}}{\mathcal{L}_{ij}\mu}\right)^{-1}. \tag{26}$$

Table 1

Key Parameters and Schematic Views for the Three Case Studies

Case	Porosity, ϕ (−)	Permeability, k (m^2)	Contact angle, θ (°)	Evaporation flux, $\mathcal{J}$ (kg s^{-1} m^{-2})	Redistribution number, Γ (−)	Numerical domain
Case 1	0.67	2.33×10^{-8}	40	-3×10^{-3}	7.47×10^{-7}	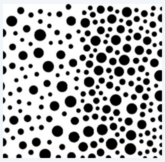
Case 2	0.67	2.33×10^{-8}	40	-1×10^{-1}	2.49×10^{-5}	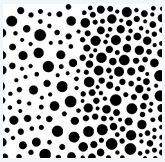
Case 3	0.47	1.89×10^{-8}	40	-3×10^{-3}	∞	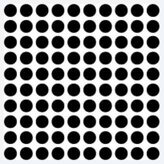

The dimensionless number Γ determines whether the redistribution of the fluid inside the porous medium is dominated by evaporation or capillarity, which is the key focus of this study. Large Γ indicates evaporation dominance, causing a steady decrease in saturation without redistribution of the fluid. Small Γ indicates capillary forces are dominating and fluid will be redistributed from the low capillarity regions to the high capillarity zones.

2.3. Numerical Domains and Boundaries

To investigate the drying dynamics in porous media, we introduced five distinct case studies, each specifically designed to examine the interplay between evaporation and capillary effects and their impact on progression of the drying front. In all scenarios, the medium is initially fully saturated with water and is in direct contact with supercritical CO_2 ($ScCO_2$) at the top boundary.

Cases 1 and 2 involve two vertical layers, with fine pores at right side and the coarse pores at the left side. For the Case 1, a low evaporation rate represents a small Γ value (refer to Equation 26), emphasizing the dominance of capillary forces. Conversely, Case 2 features a higher evaporation rate, leading to a large Γ value where evaporation effects are dominant. Case 3 examines a homogeneous porous medium with uniform pore sizes and a low evaporation rate. In this scenario, the absence of heterogeneity ensures that the capillary term in Equation 26 is zero. Detailed information for each case is provided in Table 1.

Two-dimensional simulations were conducted on a 1000 × 1000 lattice grid, representing a physical domain size of 2 mm × 2 mm, with each lattice unit corresponding to 2 μm. The physical properties of CO_2 and water used in these simulations are detailed in Table 2.

While the 2D simulations provided valuable insights into the role of evaporation rates and capillary effects, they cannot capture the connectivity of corner flow of the wetting phase. To address this limitation and explore the importance the three-dimensional connectivity of the pore space in evaporation rates, a realistic three-dimensional domain was also considered. The numerical domain was obtained from a micro-CT scan of actual rock sample from the Lower Cretaceous fluviatile sands (Haruzi et al., 2019). The simulations were performed on a lattice grid with dimensions of 300 × 300 × 300, corresponding to a physical domain of 0.6 mm × 0.6 mm × 0.6 mm, where each lattice unit represents 2 μm Figure 4 visually represents the rock's geometry, including the dimensions and specified boundary conditions. The physical properties of CO_2 and water used in these simulations are detailed in Table 2.

Table 2
Physical Properties of Water and Supercritical CO_2 at $T = 323$ K and $P = 10$ MPa

Physical property	Value
Density (kg m^{-3}) (Lemmon et al., 2010)	$\rho_{\mathrm{water}} = 992.38$ $\rho_{\mathrm{scCO}} = 386.77$
Viscosity (Pa s) (Lemmon et al., 2010)	$\mu_{\mathrm{water}} = 5.44 \times 10^{-4}$ $\mu_{\mathrm{scCO}} = 2.79 \times 10^{-5}$
Interfacial tension (mN m^{-1}) (Georgiadis et al., 2010)	$\sigma_{\mathrm{water\text{-}scCO_2}} = 26.2$
Density Ratio	$\rho_{\mathrm{water}}/\rho_{\mathrm{scCO_2}} = 2.56$
Viscosity Ratio	$\mu_{\mathrm{water}}/\mu_{\mathrm{scCO_2}} = 19.35$

To investigate the effect of evaporation rate on drying dynamics in 3D porous media, we simulated Cases 4 and 5 under identical conditions, differing only in their evaporation rates, set at -8×10^{-2} and -6.4×10^{-1} kg m^{-2} s^{-1}, respectively. The imposed constant areal fluxes $\mathcal{J}$ are consistent, in order of magnitude, with near-well drying under $scCO_2$ when combining reported CO_2 throughputs in core-flooding experiments with equilibrium H_2O-in-CO_2 solubilities at reservoir P–T (Sokama-Neuyam et al., 2023; Spycher et al., 2003). To highlight regime separation in Γ and probe the evaporation-dominated limit, we also include magnified high-$\mathcal{J}$ cases. For both 2D and 3D cases the lateral and bottom boundaries are impermeable no-slip walls (bounce-back) for both lattices. The top boundary is an open reservoir outlet for the gas lattice that maintains dry CO_2 conditions (pressure/density fixed at ρ_g^{res}; zero-gradient tangential velocity).

3. Results and Discussion

3.1. Validation of the Model

We validate the VoF–LBM in three steps of increasing realism: (a) The hydrodynamics were validated against the analytical solution for the velocity field in co-current layered two-phase flow with extreme differences in density and viscosity in a channel, (b) evaporation–capillarity coupling in a simple, solvable geometry (interconnected capillaries); and (c) a pore-scale micromodel experiment.

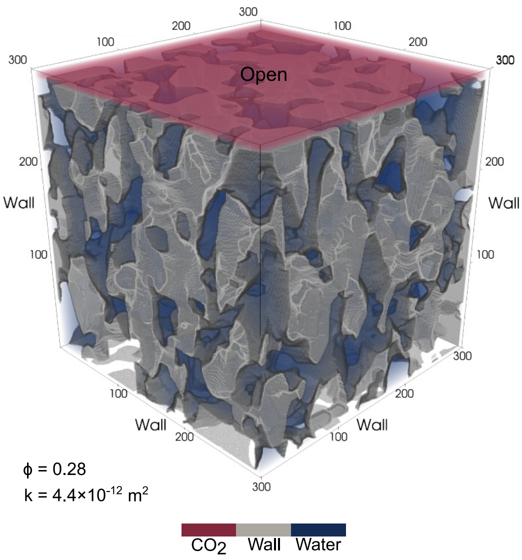

Figure 4. Geometry of the rock sample derived from micro-CT scans, showing the dimensions and boundary conditions used in the 3D simulations.

3.1.1. Validation Against the Analytical Solution for the Velocity Field in Co-Current Layered Two-Phase Flow in a Channel

The VoF-LBM two-phase flow was validated using a two-layer co-current flow of two fluids with extreme density and viscosity differences. The system consisted of two immiscible fluid layers driven by a uniform body force, equivalent to a constant pressure gradient, within a horizontal channel bounded by no-slip walls. Under these conditions, a steady stratified flow was established, with the denser fluid occupying the lower half of the channel and the lighter fluid the upper half.

As illustrated in Figure 5a, the computational domain was a plane channel of height W, with walls located at $y = 0$ and $y = W$, and periodic boundaries applied in the streamwise direction. The initial interface between the two fluids was flat and positioned at mid-channel ($y = W/2$). The lower layer represented water with $\rho_1 = 1000$ kg m^{-3} and $\nu_1 = 10^{-3}$ m^2 s^{-1}, while the upper layer represented air with $\rho_2 = 1$ kg m^{-3} and $\nu_2 = 10^{-2}$ m^2 s^{-1}, corresponding to a density ratio of 1000:1 and a viscosity ratio of 10:1. An

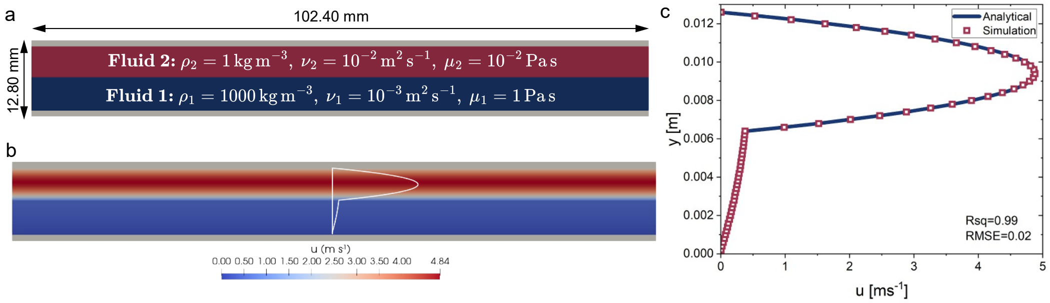

Figure 5. Two-phase co-current channel validation at high property contrast ($\rho_2/\rho_1 = 10^{-3}$, $\nu_2/\nu_1 = 10$). (a) Geometry and material properties; (b) streamwise velocity contour; (c) velocity profile: simulation (symbols) versus analytical (solid) from Equation 27.

analytical solution for the steady velocity distribution yields a piecewise parabolic (Poiseuille) profile in each layer, with velocity and shear stress continuous at the interface. The steady velocity is given by Equation 27 (Durst, 2008):

$$u(y) = \begin{cases} -\dfrac{W^2}{8\,\mu_1}\dfrac{dp}{dx}\left[\dfrac{4\mu_1}{\mu_1+\mu_2} + \dfrac{2(\mu_1-\mu_2)}{\mu_1+\mu_2}\left(\dfrac{2y}{W}-1\right) - \left(\dfrac{2y}{W}-1\right)^2\right], & 0 \le y \le \dfrac{W}{2}, \\ -\dfrac{W^2}{8\,\mu_2}\dfrac{dp}{dx}\left[\dfrac{4\mu_2}{\mu_1+\mu_2} + \dfrac{2(\mu_1-\mu_2)}{\mu_1+\mu_2}\left(\dfrac{2y}{W}-1\right) - \left(\dfrac{2y}{W}-1\right)^2\right], & \dfrac{W}{2} \le y \le W. \end{cases} \tag{27}$$

Figure 5b reports the streamwise velocity contour at steady state. Figure 5c overlays the simulated wall-normal velocity profile (symbols) with the analytical prediction from Equation 27 (solid line), showing excellent agreement: the error is within a few percent in RMSE (and $R^2 > 0.997$ across grids), with differences confined near the walls and interface as expected. This confirms that the model accurately resolves two-phase co-current channel flow even under large property contrasts.

3.1.2. Validation Against the Analytical Solution for Evaporation in Two Inter-Connected Capillaries

To validate the VOF-LBM for evaporation under capillary and gravitational effects, we analyze the drying process in two interconnected capillary tubes. Figure 3a provides a schematic view of the system, illustrating the setup and the dynamic interaction between the two tubes during the drying process. Two vertical capillary tubes with radii of R_1 and R_2 connected at the base were considered. Heights of liquid with viscosity μ in both tubes are denoted as $h_1(t)$ and $h_2(t)$.

A full derivation of this solution-including governing equations, assumptions, and nondimensionalization can be found in Appendix B, see Equations B7–B9. Here we only recall nondimensional time-dependent ODE for the height difference $\Delta h(t)$ and the steady-state (Jurin) limit used for validation.

$$\frac{d\xi}{d\tilde{t}} = \frac{\lambda\pi\left(1+\lambda^2\right)^2(\mathrm{Bo}\;\xi\lambda + 2 - 2\lambda)}{8\left[\pi\xi\left(1-\lambda^6\right) + \left(1+\lambda^4\right)\left(\tilde{\mathcal{J}}\left(1+\lambda^2\right) - \tilde{V}_0\right)\right]},\; \tilde{\mathcal{J}}\left(1+\lambda^2\right) - \tilde{V}_0 < 0 \tag{28}$$

where the following nondimensional numbers have been used:

$$\xi = \frac{\Delta h}{R_1}, \quad T_c = \frac{\mu R_1}{\sigma\cos\theta}, \quad \tilde{t} = \frac{t}{T_c}, \quad \lambda = \frac{R_2}{R_1}, \quad Bo = \frac{\rho g R_1^2}{\sigma\cos\theta}, \quad \tilde{\mathcal{J}} = \frac{J\pi t}{\rho R_1}, \quad \tilde{V}_0 = \frac{V_0}{R_1^3}. \tag{29}$$

Setting $d\xi/d\tilde{t} = 0$ in the nondimensional equation yields:

$$\Delta H_{\mathrm{eq}} = \frac{2(\lambda-1)}{Bo\;\lambda}, \tag{30}$$

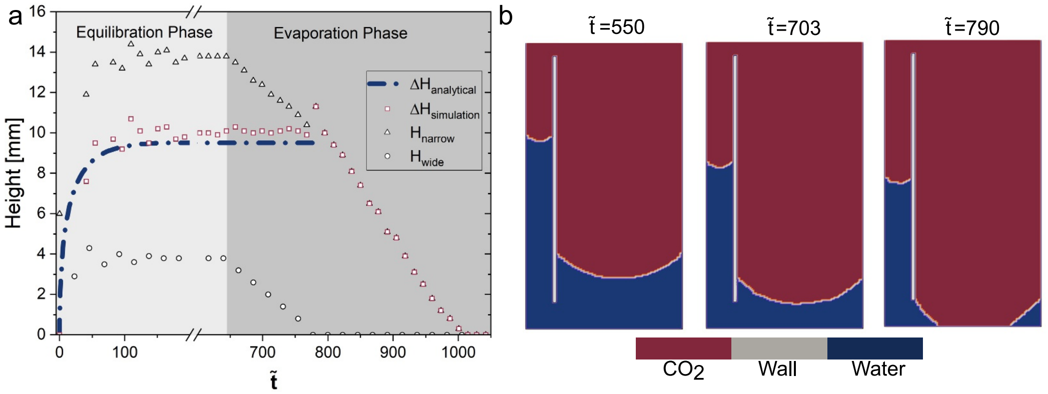

Figure 6. (a) Height of the capillary interface in the capillary tubes over time. The plot also shows the calculated ΔH in simulation and the analytical value of ΔH using Equation 28. (b) Simulation snapshots of drying in two interconnected capillary tubes with different widths at various times.

which, in dimensional form, gives Jurin's law

$$\Delta H_{\mathrm{eq}} = \frac{2\sigma\cos\theta}{\rho g}\left(\frac{1}{R_1} - \frac{1}{R_2}\right). \tag{31}$$

We compare simulations against this prediction and against the time-dependent solution evaluated from Equation 28.

When the initial nondimensional height difference is set to zero ($\xi(0) = 0$), both tubes have the same liquid level. Under this condition, ξ increases over time, approaching the equilibrium value ξ_{eq} determined by the balance of capillary, evaporation, and hydrostatic pressures. This increase is driven by the capillary pressure difference due to the differing radii of the tubes and evaporation rate.

The theoretical formation presented in Appendix B forms the basis for validating the VOF-LBM. Water movement was simulated in two inter-connected capillary tubes with diameters of 1.5 and 9.1 mm, respectively. The contact angle was set to 40°. Under the equilibrium conditions, water rises higher in the narrower tube. The difference in water heights between the two tubes (ΔH) is compared against the analytical Equation 28. After reaching the capillary equilibrium, evaporation was initiated.

Figure 6a shows the height of capillary interface in each tube over time, along with the calculated ΔH and the analytical value of ΔH. The plot demonstrates that after evaporation begins, the model successfully maintains a nearly constant (ΔH) with a deviation of less than 3% illustrating the accuracy and robustness of the simulation. Figure 6b presents snapshots of the process at different stages, showing the distribution of water in both tubes as evaporation proceeds. A grid-independence study for this configuration is provided in Appendix C (see Figure C1), confirming monotonic convergence.

According to the theoretical analysis and Equation 28, if the initial height difference (ΔH) is at equilibrium (ΔH_{eq}), this height difference during evaporation remains constant. This behavior arises because, at equilibrium, the capillary and gravitational forces are balanced, and the height difference remains constant even as water evaporates from both tubes. This comparison confirms the capability of the model to accurately simulate capillary dynamics during evaporation, as predicted by the theoretical analysis.

3.1.3. Validation Against Evaporation of a Water Cluster in a Micromodel Experiment

We further validated the coupled VoF–LBM model using an isolated water cluster extracted from the micromodel experiments of Yan et al. (2025). All experimental procedures and imaging details are given in Yan et al. (2025); here we used their original image sequence and selected a single, well-isolated cluster to enable a one-to-one comparison.

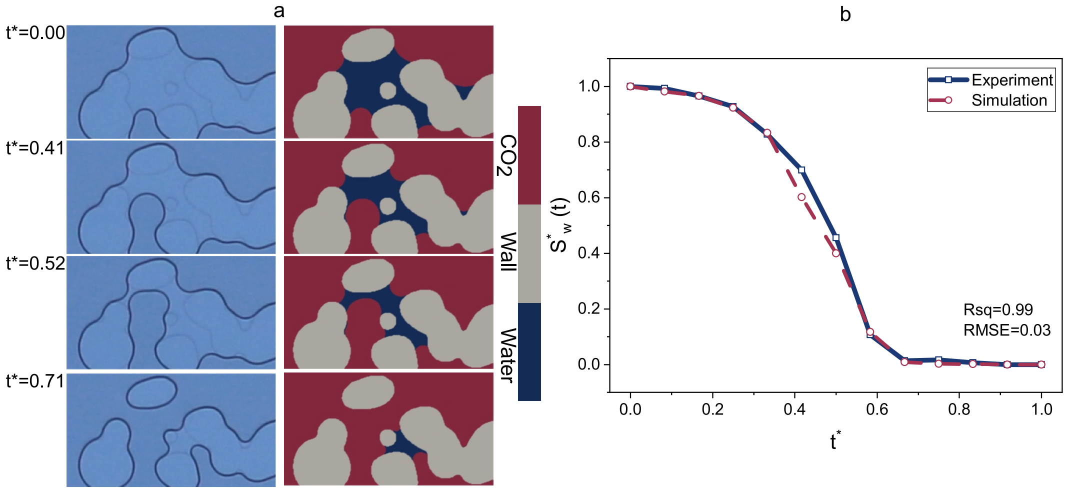

Figure 7. Validation against evaporation of a water cluster in a micromodel experiment Yan et al. (2025). (a) Experiment (left) versus simulation (right) at matched times; the model reproduces pinning in narrow constrictions and preferential advance in larger pores. (b) Water saturation $S_w^*(t)$ in the common field of view.

Operating conditions and domain were matched to the experiment: pressure 18.3 kPa, temperature $T \approx 32\,^\circ\mathrm{C}$, and a field of view 1138 μm × 860 μm (simulation discretized on a 614 × 464 lattice).

Figure 7a shows experiment–simulation snapshots at matched *normalized times* $t^* = (t - t_0)/(t_{\mathrm{end}} - t_0)$ over the same field of view (see also Movie S1). The model reproduces the observed behavior of pinned menisci in constrictions and preferential advance through larger pores/throats, consistent with capillary control of the drying front. Figure 7b compares the water saturation $S_w^*(t) = A(t)/A_0$ within the region of interest; the curves agree with RMSE $= 3.0\%$, and $R^2 = 0.99$). For shape-only comparison, time was also rescaled to $t^* = (t - t_0)/(t_{\mathrm{end}} - t_0)$, with t_{end} defined when $S_w < \varepsilon$ ($\varepsilon = 0.01$). The VoF–LBM captures successfully both the drying kinetics and the morphology of the interfaces of the water cluster in a micromodel.

3.2. Simulation of Drying in Porous Media

3.2.1. Morphology of the Drying Interface

Figures 8 and 9 illustrate the changes in fluid distribution across each scenario at four distinct water saturations and time intervals (see also Movies S2–S6). All simulations started from a fully saturated domain. The evaporation and capillary forces significantly influence the liquid distribution during the drying process. Despite having identical geometries, Case 1 and Case 2 exhibit different fluid distributions due to variations in evaporation rates fast in Case 2 and slow in Case 1, as reflected in Γ values in Table 1. In Case 1, while evaporation takes place from all interfaces, drying front recedes in the coarse region at first (drainage) due to the capillary suction in the fine region (imbibition). In Case 2, $\Gamma = 2.49 \times 10^{-5}$, the evaporation forces are dominant, resulting in a more uniform movement of the drying front across both fine and coarse regions of the porous media. In Case 3, $\Gamma = \infty$ the homogeneous pore structure eliminates the influence of capillary pressure gradient due to $\Delta r_p = 0$, making the fluid distribution entirely dependent on the evaporation rate. Results demonstrate that without heterogeneity, the drying front is more stable and its movement is controlled by the evaporation rate. Figure 8 illustrates the temporal evolution of water saturation over the entire domain for 2D cases. In Case 1, for small Γ, the saturation decreases nonlinearly over time. In contrast, Cases 2 and 3 exhibit a linear saturation decrease due to the high evaporation rate, stable amount of fluid-fluid interfacial area.

A similar simulation was performed on a 3D domain, representing Cases 4 and 5. Introducing the third dimension significantly increases the complexity of the pore geometry and widens the distribution of pore sizes. To illustrate the difference between the two cases more clearly, we first compare them at the same global water saturation, ensuring that differences are not simply due to different overall drying rates. For each saturation-matched pair of frames, we build binary water masks and a signed voxelwise difference $\mathcal{D}$: $\mathcal{D} = +1$ where a voxel is wet in Case 5 but dry in Case 4, $\mathcal{D} = -1$ where it is wet in Case 4 but dry in Case 5, and $\mathcal{D} = 0$ if both are dry or wet. We then

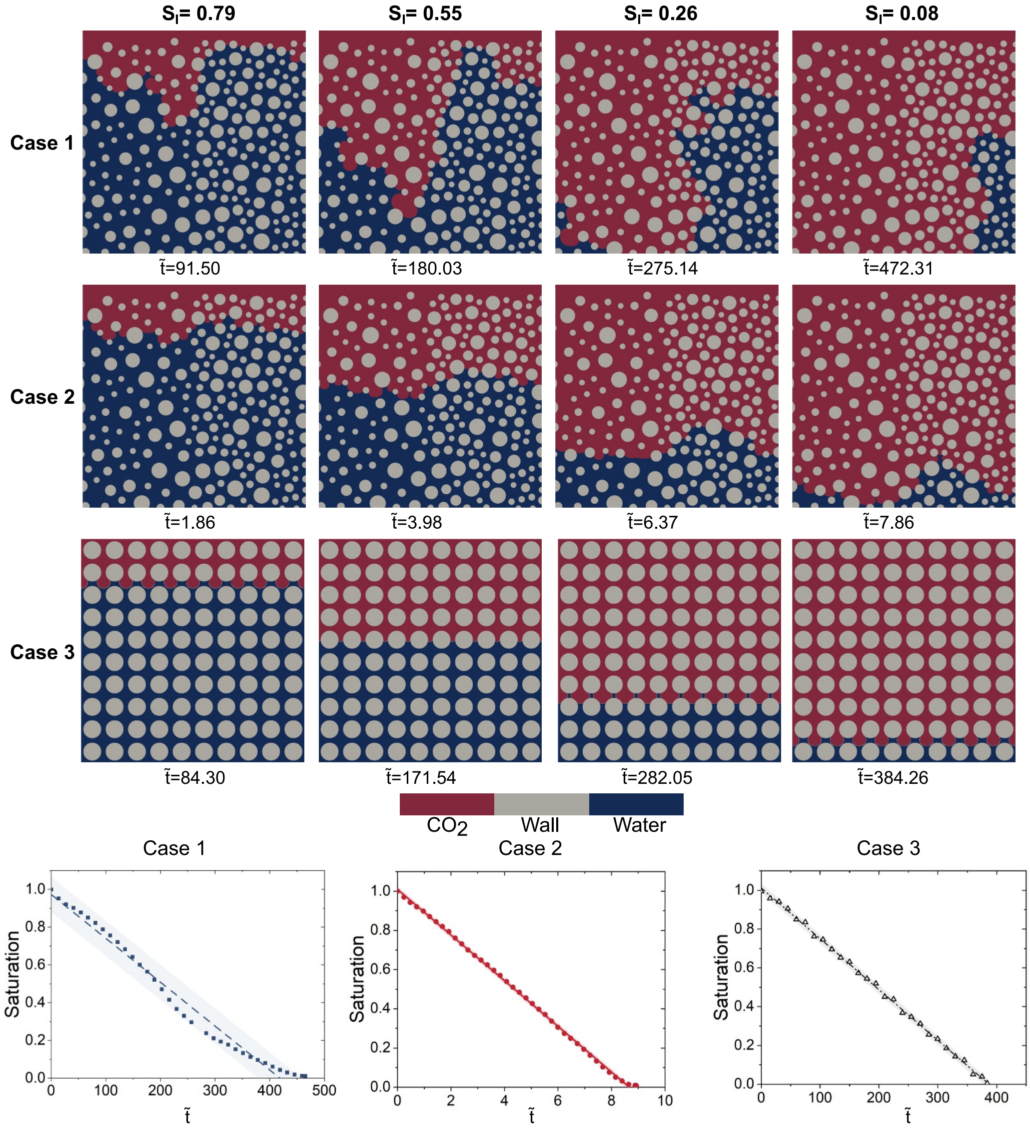

Figure 8. 2D simulation snapshots of CO_2-water distribution at four water saturations and corresponding time intervals during the drying process, alongside the temporal evolution of water saturation across the entire domain during the drying process. These images provide a visual comparison of fluid behavior across the Cases 1 to 3. Refer to Movies S1–S3 for dynamic visualisations.

compute the spatial mean $\langle \mathcal{D} \rangle$ over the field of view for that pair and group these values by S_w (Figure 10). By construction, $\langle \mathcal{D} \rangle < 0$ indicates that more voxels are dry in Case 5 while still wet in Case 4 (a more spatially advanced, uniform front in Case 5), whereas $\langle \mathcal{D} \rangle > 0$ indicates the opposite. The box plots (25%–75% with whiskers ±1.5 IQR) show: at high saturation [0.8,1.0] the distribution is narrow and centered near zero (nearly identical early patterns); through the mid range [0.6,0.8] and [0.4,0.6] the medians shift slightly negative, evidencing earlier local drying in Case 5 while Case 4 retains isolated wet pockets; at [0.2,0.4] the negative bias persists but weakens; in the late, residual stage [0,0.2] the spread increases markedly and the median moves slightly above zero, reflecting heterogeneous post-front clusters that can persist in either case. Overall, at matched S_w the mid-stage bias toward $\langle \mathcal{D} \rangle < 0$ supports a more uniformly advanced front in Case 5, whereas Case 4 exhibits stronger local retention; late-stage variability is dominated by fragmented residuals.

The competition between evaporation and capillarity can be demonstrated through internal capillary pressure (by average of the curvature of interfaces). Figure 11 presents the average capillary head as a function of water saturation for two half domains in Cases 1–3 for the coarse and fine domains at global water saturation of 0.53.

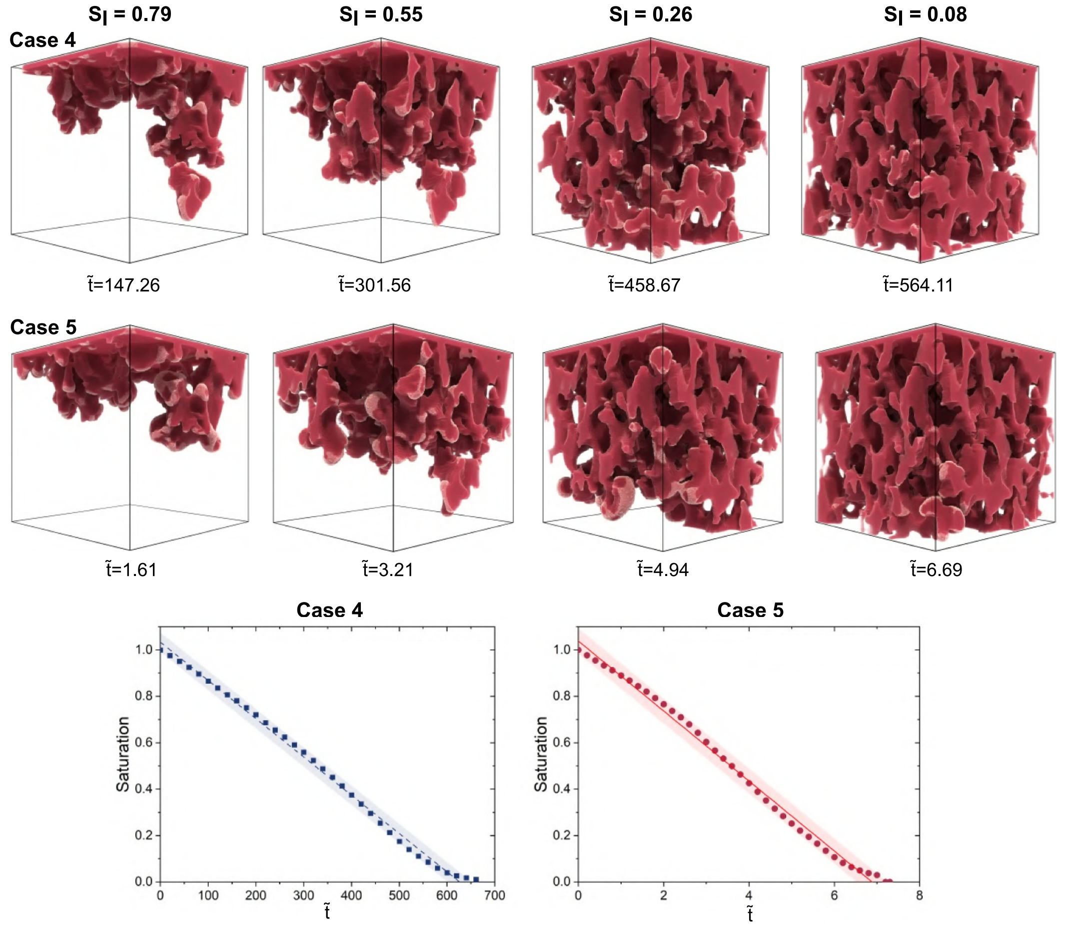

Figure 9. 3D simulation snapshots of CO_2-water distribution at four saturations and corresponding time intervals during the drying process, alongside the temporal evolution of water saturation across the entire domain during the drying process. Cases 4 represents a smaller evaporation rate compared to the Case 5). Refer to Movies S5 and S6 for dynamic visualisations.

Capillary head is used here in the hydraulic sense: it is the pressure head associated with capillary pressure, that is, the height of a water column that would balance the capillary pressure. We report it in length units (mm). This follows the convention used in pore-scale drying analyses (e.g., Lehmann and Or (2009)). In heterogeneous media, such as Cases 1 and 2, the fine regions exhibit a higher capillary pressure compared to the coarse regions. Due to the smaller evaporation rate (smaller Γ), the capillarity behaves similar to an equilibrium case. As the evaporation rate increases, the dynamics of evaporation is much faster (large Γ) the difference between the capillary forces between the two zones is much smaller.

3.2.2. Redistribution of Water Due To Capillarity

One the key questions which is relevant to the drying during CO_2 injection is related to the capillary-induced backflow (Norouzi et al., 2021; Pruess & Müller, 2009). It was shown that capillary forces such brine to the evaporation sites and the salt precipitation grows significantly with time. To understand better the impact of heterogeneity (Δr_p) and evaporation rate of water redistribution, we have investigated the historical heatmap of magnitude of water velocity for Cases 1–3.

Figure 12a presents contour plots historical heat map of velocity magnitudes. For each lattice node $\mathbf{x}$ we form a time-averaged liquid-phase velocity $\bar{\mathbf{u}}(\mathbf{x}) = \frac{1}{N}\sum_{n=1}^{N}\mathbf{u}(\mathbf{x}, t_n)$ over the full run, and visualize $|\bar{\mathbf{u}}|$ together with streamlines of $\bar{\mathbf{u}}$ to reveal persistent pathways of water redistribution. In Case 1, $\Gamma = 7.47 \times 10^{-7}$, capillary forces induce substantial water movement and capillary suction toward the fine domain. This pronounced redistribution underscores the dominant influence of capillarity heterogeneity, Δr_p, in driving water

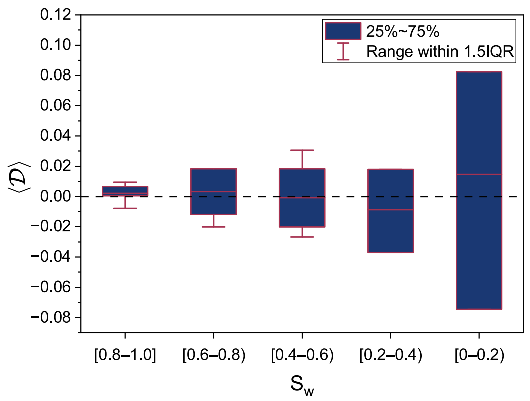

Figure 10. Distribution of the spatially averaged difference $\langle \mathcal{D} \rangle$ between saturation-matched frames (Case 5 vs. Case 4) across S_w bins. For $\langle \mathcal{D} \rangle < 1$ more voxels are dry in Case 5 (larger evaporation rate) while still wet in Case 4 (smaller evaporation rate). Difference between two cases gets larger with decrease of water saturation.

redistribution. In contrast, Case 2, characterized by elevated evaporation rates, $\Gamma = 2.49 \times 10^{-5}$, exhibits a marked reduction in water velocity and reduced redistribution of water. Case 3, which features a homogeneous porous structure, $\Delta r_p = 0$, demonstrates an almost complete cessation of water redistribution, highlighting the critical role of heterogeneity in facilitating capillary-mediated flow.

For a more quantitative analysis of water velocities, Figure 12b presents the distribution of the water velocity magnitudes at three distinct saturations for Cases 1–3. The data reveal that at lower saturations, water redistribution becomes increasingly pronounced across Cases 1 and 2 due to large spatial gradients in capillary forces across the interfaces. Specifically, in Case 1, lower saturation intensifies the existing capillary forces, resulting in more vigorous fluid movement. Conversely, in Case 2, while higher evaporation rates generally suppress redistribution, lower saturation levels partially mitigate this effect, allowing for some degree of capillary-driven flow. Case 3 continues to exhibit minimal redistribution even at lower saturations, reinforcing the notion that structural homogeneity inherently limits capillary-induced fluid movement. These simulation results offer new insights into the impact of pore size heterogeneity and evaporation rates during CO_2 injection into saline aquifers. The findings suggest that as water saturation decreases, pore size heterogeneity plays a more prominent role, and capillary backflow becomes increasingly significant in transporting salt to the zones of salt precipitation.

4. Conclusions

This paper addresses the coupled phenomena of evaporation and two-phase flow in porous media, focusing on fluids with extreme viscosity and density contrasts. It has two key contributions: (a) the development of a novel lattice Boltzmann (LB) model capable of simulating coupled evaporation and capillary-driven two-phase flow in porous media under such extreme physical contrasts, and (b) new insights into the role of heterogeneity and capillary effects in controlling evaporation dynamics and water redistribution.

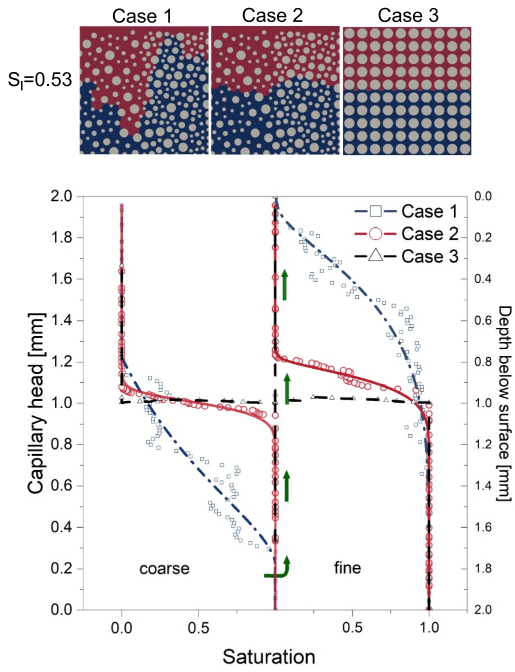

Figure 11. Capillary head and distance from the evaporating surface over saturation at the global water saturation of 0.53. Blue squares (Case 1), red circles (Case 2), and black triangles (Case 3) represent point data for capillary head and depth in fine and coarse regions. The corresponding blue, red, and black lines are fitted curves using the Skjaeveland (Skjaeveland et al., 2000) capillary pressure-saturation equation.

The study investigates how water is redistributed in porous media under the combined influence of capillarity and evaporation, a problem relevant to CO_2 injection into saline aquifers for geological carbon storage. Experimental studies have shown that during brine evaporation, capillary action continuously supplies water to salt precipitation zones. To better understand this process, particularly the evolution of the drying front and water redistribution due to capillarity, a robust pore-scale model is required. The lattice Boltzmann method (LBM) was employed as the modeling framework because of its ability to handle complex geometries and multiphase flow dynamics. However, existing LB models for drying in porous media have been limited by their inability to resolve sharp interfaces or account for large viscosity and density contrasts. To overcome these limitations, a Volume of Fluid (VOF)-based LBM was developed to simulate two-phase flow with coupled evaporation processes. To the best of our knowledge, this is the first LBM framework capable of capturing drying in porous media with sharp interfaces under such extreme physical property contrasts, representative of CO_2–water systems.

To validate the developed model, three validations against analytical equations as well as evaporation in a micromodel were carried out. After successful validation, the model was applied to two- and three-dimensional drying simulations that included the effects of pore size heterogeneity, capillary pressure gradients, and evaporation. A dimensionless number was

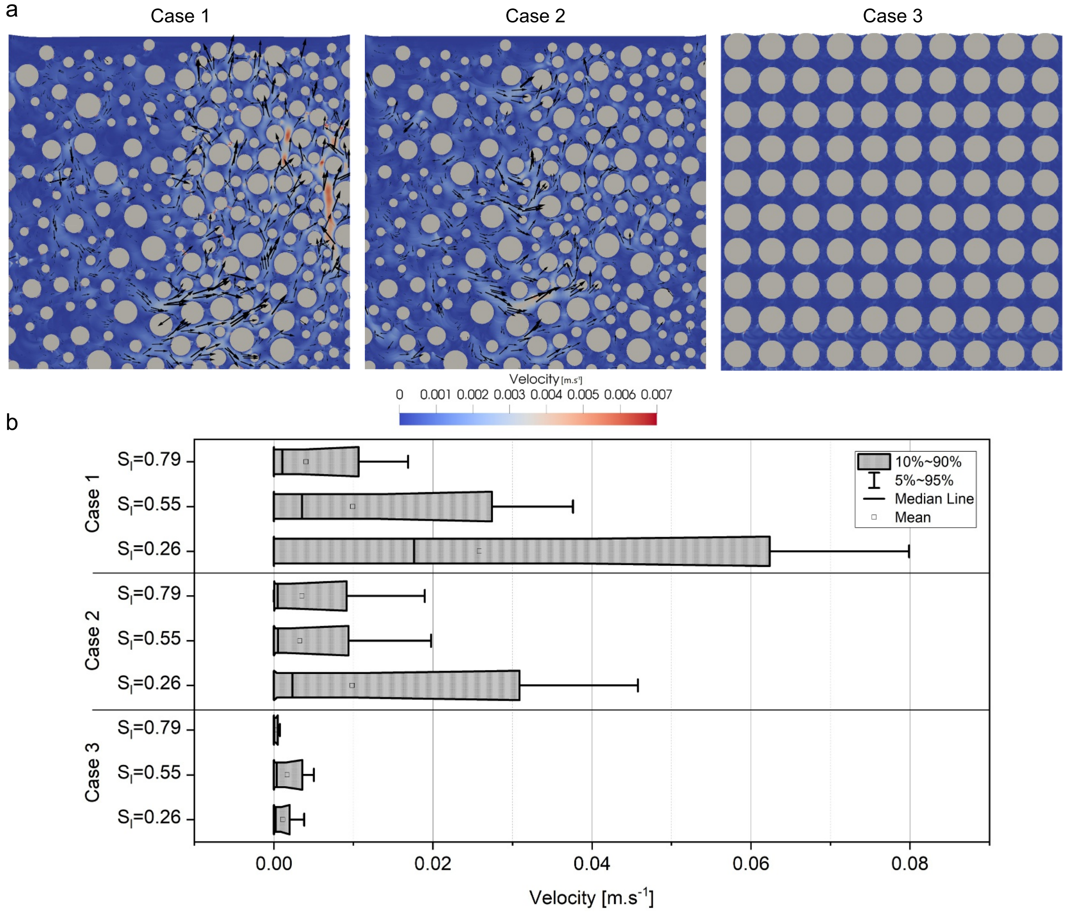

Figure 12. (a) Historical heat map of water velocity magnitude for 2D case studies. (b) Statistical distribution of water velocity magnitude at three saturations for Cases 1–3.

introduced to characterize the relative importance of evaporation-driven mass transfer compared with capillary-induced flow. This parameter allowed for quantitative comparison among different simulation scenarios.

The results show that the interaction between evaporation rate and capillary pressure gradient governs the morphology of the drying front and the redistribution of water within the porous structure. When evaporation flux dominates over capillary-induced water flow, the drying front remains stable and nearly linear. In contrast, stronger capillary gradients, such as those found in fine–coarse heterogeneous media, lead to nonlinear drying front evolution and significant water redistribution. Pore size heterogeneity was identified as a dominant factor: variations in capillary pressure cause uneven drying, with fine pores retaining liquid for longer periods. This mechanism promotes localized salt precipitation and can reduce injectivity in CO_2 storage formations. The developed LB model successfully addresses the limitations of previous approaches by accurately resolving sharp interfaces and incorporating realistic physical contrasts. It provides a powerful tool for investigating two-phase flow, evaporation, and salt deposition in porous media. Simulations in three-dimensional domains further revealed that increased connectivity of the liquid phase significantly amplifies capillary-driven water redistribution compared with two-dimensional cases. The three-dimensional results highlight the importance of liquid connectivity in the three-dimensional space. These findings improve our understanding of the mechanisms governing salt precipitation and drying during CO_2 injection into saline aquifers and contribute to a more complete description of evaporation, capillarity, and fluid redistribution in porous media under realistic subsurface conditions.

Nomenclature

The following symbols and acronyms are used throughout this study.

Symbol	Description	Units
Latin Symbols		
$\mathbf{x}$	Position vector	m (or lu)
t	Time	s (or lu)
$\mathbf{u}$	Macroscopic fluid velocity	m s^{-1}
c_s	Lattice speed of sound	lu step^{-1}
f_i	Particle distribution function in direction i	–
f_i^{eq}	Equilibrium distribution in direction i	–
$\mathbf{f}$	Vector of distributions	–
$\mathbf{m}$	Moment vector	–
$\mathbf{m}^{\text{eq}}$	Equilibrium moment vector	–
$\mathbf{M}$	Transformation matrix (distributions → moments)	–
$\mathbf{S}$	Diagonal relaxation matrix in MRT	–
$\mathbf{c}_i$	Discrete lattice velocity for direction i	lu step^{-1}
w_i	Lattice weight for direction i	–
$\mathbf{F}$	External or body force	N
$\mathcal{J}$	Evaporation mass flux	kg m^{-2} s^{-1}
$\dot{m}$	Interfacial mass transfer rate (per interface cell)	kg s^{-1}
$\dot{m}''$	Evaporation flux per unit area	kg m^{-2} s^{-1}
$\mathcal{A}_{ij}$	Interface area between domains i and j	m^2
$Q_{ij}(t)$	Capillary-driven water volumetric flux between i and j	m^3 s^{-1}
ΔP	Pressure difference driving flow	Pa
$h_i(t)$	Liquid height in domain/tube i	m
A_{int}	Per-cell interfacial area	m^2
Δt	Time step	s
Δx	Lattice spacing	m
k	Intrinsic permeability	m^2
ϕ	Porosity	–
θ_{eq}	Equilibrium contact angle	°
$\mathcal{R}_{\text{total}}$	Total flow resistance (two-tube model)	Pa s m^{-3}
T_c	Visco-capillary characteristic timescale	s
$\mathbf{u}_I$	Interfacial (liquid-side) velocity	m s^{-1}
$\mathbf{n}$	Unit normal (from continuous to dispersed phase)	–
$U_c,\ U_d$	Normal velocity components on c and d sides	m s^{-1}
Greek Symbols		
ρ	Fluid density	kg m^{-3}
ρ_ℓ	Liquid density	kg m^{-3}
ρ_g	Gas density	kg m^{-3}
μ	Dynamic viscosity	Pa s
$\mu_c,\ \mu_d$	Dynamic viscosities (continuous c, dispersed d)	Pa s

Continued

Symbol	Description	Units
ν	Kinematic viscosity	$\mathrm{m}^2\ \mathrm{s}^{-1}$
σ	Surface tension	$\mathrm{N\ m}^{-1}$
ϵ	Cell filling fraction (m/ρ)	–
α	Interface classification threshold	–
χ_Γ	Interface indicator (1 at interface, else 0)	–
$\tilde{t}$	Nondimensional time	–
$\boldsymbol{\zeta}$	Microscopic particle velocity	$\mathrm{m\ s}^{-1}$
s_ν	Shear-mode relaxation rate in MRT	–
ΔH_{eq}	Equilibrium height difference (nondimensional)	–
Subscripts and Superscripts		
ℓ	Liquid phase (subscript)	–
g	Gas phase (subscript)	–
c	Continuous (liquid) side of interface	–
d	Dispersed (gas) side of interface	–
eq	Equilibrium value	–
I	Interface quantity	–
Acronyms		
LBM	Lattice Boltzmann Method	–
LBE	Lattice Boltzmann Equation	–
MRT	Multiple-Relaxation-Time model	–
VOF	Volume-of-Fluid	–
CE	Chapman–Enskog expansion	–
CCS	Carbon Capture and Storage	–
CT	Computed Tomography (micro-CT)	–
RMSE	Root Mean Square Error	–

Appendix A: Chapman–Enskog Derivation of the Evaporation Model

This appendix provides the Chapman–Enskog (CE) derivation showing that the discrete two-lattice MRT-LBM with evaporation recovers the correct macroscopic equations for each phase. The evaporation source produces a localized mass sink/source in the continuity equation and, under appropriate moment constraints and time-centering, does not introduce a spurious force in the momentum balance.

For each phase $(\cdot) \in \{\ell, g\}$, the MRT-LBM with external forcing and evaporation is

$$f_i^{(\cdot)}(\mathbf{x}+\mathbf{c}_i\Delta t, t+\Delta t) - f_i^{(\cdot)}(\mathbf{x},t) = -\left[\mathbf{M}^{-1}\mathbf{S}\right]_{ij}\left(m_j^{(\cdot)} - m_j^{(\cdot),eq}\right) + \left(\mathbf{I} - \frac{1}{2}\mathbf{M}^{-1}\mathbf{S}\mathbf{M}\right)\left(F_i^{(\cdot)} + S_i^{(\cdot),\mathrm{evap}}\right), \tag{A1}$$

where $f_i^{(\cdot)}$ are the populations, $\mathbf{M}$ maps to moment space, $\mathbf{S}$ is diagonal (MRT), $F_i^{(\cdot)}$ are body-force terms, and $S_i^{(\cdot),\mathrm{evap}}$ represents interfacial mass transfer. The prefactor $\left(\mathbf{I} - \frac{1}{2}\mathbf{M}^{-1}\mathbf{S}\mathbf{M}\right)$ provides second-order time-centering; in our implementation this factor is absorbed into the definitions of $F_i^{(\cdot)}$ and $S_i^{(\cdot),\mathrm{evap}}$.

The evaporation source is confined to interface cells and satisfies the zeroth- and first-moment constraints

$$\sum_i S_i^{\ell,\text{evap}} = -\chi_\Gamma\ \dot{m}, \qquad \sum_i \mathbf{c}_i S_i^{\ell,\text{evap}} = -\chi_\Gamma\ \dot{m}\ \mathbf{u}_I, \tag{A2}$$

$$\sum_i S_i^{g,\text{evap}} = +\chi_\Gamma\ \dot{m}, \qquad \sum_i \mathbf{c}_i S_i^{g,\text{evap}} = +\chi_\Gamma\ \dot{m}\ \mathbf{u}_I, \tag{A3}$$

where χ_Γ indicates interface cells and $\mathbf{u}_I$ is the interface velocity. Using the same $\mathbf{u}_I$ for both phases guarantees exact global momentum conservation. We treat $\dot{m}$ as a volumetric mass-transfer rate (kg m^{-3} s^{-1}); if an interfacial areal flux $\dot{m}''$ (kg m^{-2} s^{-1}) is prescribed, then $\dot{m} = a_\Gamma \dot{m}''$ with a_Γ the interfacial area density (m^2/m^3).

Introduce a small parameter ϵ and the multiscale expansions

$$f_i^{(\cdot)} = f_i^{(\cdot,0)} + \epsilon f_i^{(\cdot,1)} + \epsilon^2 f_i^{(\cdot,2)} + \cdots, \qquad \partial_t = \epsilon\partial_{t_1} + \epsilon^2\partial_{t_2}, \qquad \nabla = \epsilon\nabla_1, \qquad S_i^{(\cdot),\text{evap}} = \epsilon S_{i,1}^{(\cdot)}. \tag{A4}$$

At $O(\epsilon^0)$, $f_i^{(\cdot,0)} = f_i^{(\cdot),eq}\left(\rho_{(\cdot)}, \mathbf{u}_{(\cdot)}\right)$. At $O(\epsilon^1)$,

$$\partial_{t_1} f_i^{(\cdot,0)} + \mathbf{c}_i \cdot \nabla_1 f_i^{(\cdot,0)} = -\left[\mathbf{M}^{-1}\mathbf{S}\right]_{ij} f_j^{(\cdot,1)} + F_i^{(\cdot,0)} + S_{i,1}^{(\cdot)}. \tag{A5}$$

Zeroth moments give the continuity equations

$$\partial_{t_1}\rho_\ell + \nabla_1 \cdot \left(\rho_\ell \mathbf{u}_\ell\right) = -\chi_\Gamma \dot{m}, \qquad \partial_{t_1}\rho_g + \nabla_1 \cdot \left(\rho_g \mathbf{u}_g\right) = +\chi_\Gamma \dot{m}. \tag{A6}$$

First moments yield (for the liquid)

$$\partial_{t_1}\left(\rho_\ell \mathbf{u}_\ell\right) + \nabla_1 \cdot \left(\rho_\ell \mathbf{u}_\ell \mathbf{u}_\ell + c_s^2 \rho_\ell \mathbf{I}\right) = \rho_\ell\, \mathbf{F} + \mathbf{u}_I\left(-\chi_\Gamma \dot{m}\right). \tag{A7}$$

Using the material derivative and continuity,

$$\rho_\ell \frac{D\mathbf{u}_\ell}{Dt} = -\nabla_1 p_\ell + \rho_\ell\, \mathbf{F} + \left(\mathbf{u}_I - \mathbf{u}_\ell\right)\left(-\chi_\Gamma \dot{m}\right). \tag{A8}$$

Thus the interfacial recoil term cancels exactly when $\mathbf{u}_I = \mathbf{u}_\ell$ (comoving choice); otherwise, $\left(\mathbf{u}_I - \mathbf{u}_\ell\right)\left(-\chi_\Gamma \dot{m}\right)$ remains as a physical momentum-exchange term.

At $O\left(\epsilon^2\right)$, non-equilibrium moments generate viscous stresses. For MRT, the shear viscosity is

$$\nu_\ell = c_s^2\left(\frac{1}{s_\nu} - \frac{1}{2}\right)\Delta t, \tag{A9}$$

where s_ν is the shear-mode relaxation rate. A bulk-viscosity contribution arises via the bulk/energy mode; we set $s_{\text{bulk}} = s_\nu$ so that bulk effects vanish, yielding

$$\nabla \cdot \boldsymbol{\tau}_\ell = \nabla \cdot \left[\nu_\ell \rho_\ell \left(\nabla \mathbf{u}_\ell + \nabla \mathbf{u}_\ell^{\top}\right)\right]. \tag{A10}$$

Combining orders and substituting continuity, the macroscopic liquid equations are

$$\frac{\partial \rho_\ell}{\partial t} + \nabla \cdot \left(\rho_\ell \mathbf{u}_\ell\right) = -\chi_\Gamma\ \dot{m}, \tag{A11}$$

$$\rho_\ell \frac{D\mathbf{u}_\ell}{Dt} = -\nabla p_\ell + \nabla \cdot \boldsymbol{\tau}_\ell + \rho_\ell\, \mathbf{F} + \left(\mathbf{u}_I - \mathbf{u}_\ell\right)\left(-\chi_\Gamma \dot{m}\right). \tag{A12}$$

For the comoving choice $\mathbf{u}_I = \mathbf{u}_\ell$, the last term disappears and the standard Navier–Stokes form is recovered without spurious forces. The gas equations are analogous, with the opposite sign in the continuity source representing mass gain.

In summary, the CE analysis shows: (a) continuity includes a localized interfacial sink/source; (b) momentum equations are free of spurious body forces for $\mathbf{u}_I = \mathbf{u}$, with a clear physical recoil term otherwise; (c) global mass and momentum are conserved because gains in one phase equal losses in the other; and (d) with open gas boundaries, the gas behaves as a constant-pressure reservoir, consistent with near-well CO_2 injection conditions.

Appendix B: Drying in Two Interconnected Capillary Tubes

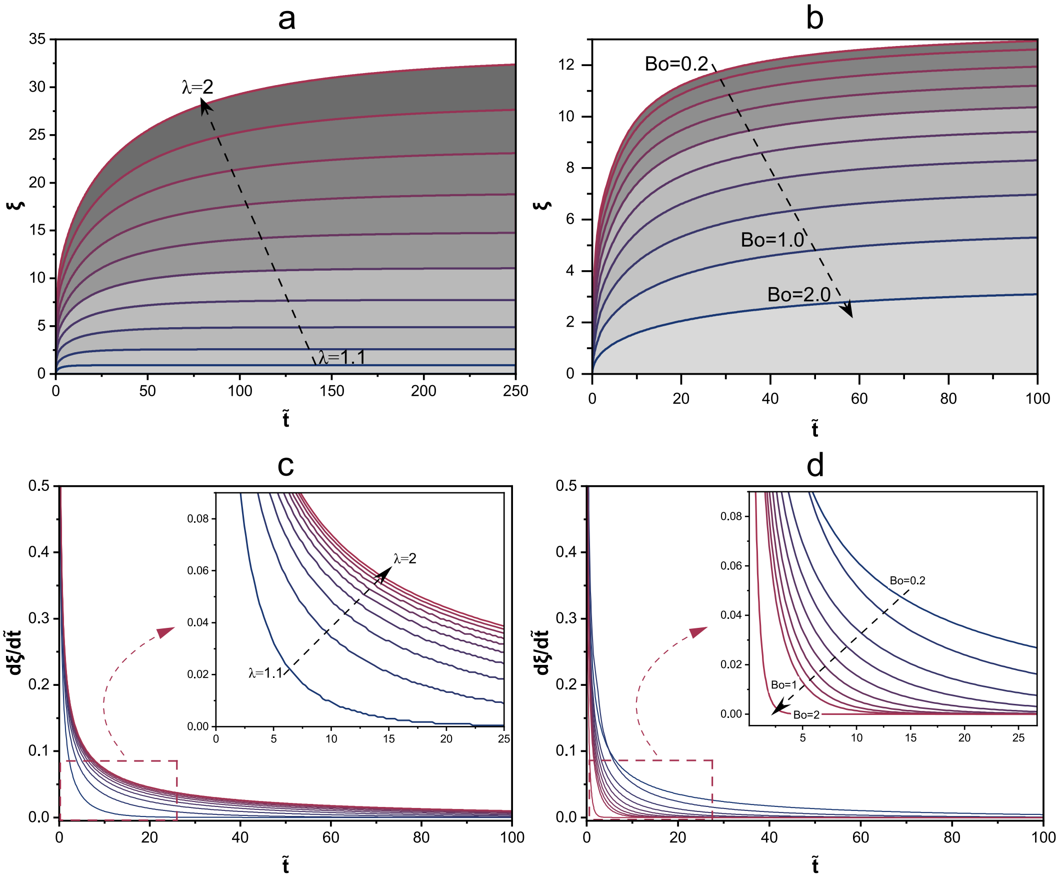

Figure B1. Evolution of the nondimensional height difference and its rate of change for specified radius ratios and Bond numbers. (a) $\xi(\tilde{t})$ for $\lambda \in \{1.1, 1.2, \ldots, 2.0\}$ at fixed $Bo = 0.2$, $\tilde{\mathcal{J}} = 10^{-6}$, and $\tilde{V}_0 = 10^{-3}$. (b) $\xi(\tilde{t})$ for $Bo \in \{0.2, 0.4, 0.6, 0.8, 1.0, 2.0\}$ at fixed $\lambda = 1.5$, $\tilde{\mathcal{J}} = 10^{-6}$, and $\tilde{V}_0 = 10^{-3}$. (c) $d\xi/d\tilde{t}$ for the same λ values as in (a). (d) $d\xi/d\tilde{t}$ for the same Bo values as in (b). All runs use the initial condition $\xi(0) = 0$ and integrate Equation B8 with a fourth-order Runge–Kutta scheme (panels a, c: $\Delta\tilde{t} = 0.05$, $\tilde{t}_{\max} = 250$; panels b, d: $\Delta\tilde{t} = 0.02$, $\tilde{t}_{\max} = 100$). The constraint $\tilde{\mathcal{J}}(1 + \lambda^2) - \tilde{V}_0 < 0$ is enforced.

The primary goal of this section is to analyze the drying process in two interconnected capillary tubes. Two vertical capillary tubes with radii of R_1 and R_2 connected at the base were considered. Heights of liquid with viscosity μ in both tubes are denoted as $h_1(t)$ and $h_2(t)$. Figure 3a provides a schematic view of the system, illustrating the setup and the dynamic interaction between the two tubes during the drying process. To estimate the mass exchange due to evaporation, gravity, and capillarity, it is needed to determine the evolution of the height difference $\Delta h(t) = h_1(t) - h_2(t)$ over time.

The volume of liquid in each tube is influenced by the capillary flux entering or exiting the tube and the evaporation flux at the interface. Capillary action governs the rise of liquid in each tube, balancing gravitational and surface tension forces. We assume evaporation occurs uniformly at the liquid-air interface, and flow between the tubes follows the Hagen-Poiseuille law under the condition of laminar, incompressible flow.

Using the Hagen–Poiseuille law, we can express the volumetric flow rate Q between the two tubes as (White, 1990):

$$Q = \frac{\Delta P}{\mathcal{R}_{\text{total}}}, \tag{B1}$$

where ΔP is the pressure difference driving the flow, and $\mathcal{R}_{\text{total}}$ is the total flow resistance of the two tubes. The total pressure difference $\Delta P(t)$ driving the flow is a sum of the hydrostatic pressure difference $\Delta P_{\text{h}}(t)$ and the capillary pressure difference ΔP_{c}:

$$\Delta P(t) = \Delta P_{\text{h}}(t) + \Delta P_{\text{c}} = \rho g\ \Delta h(t) + 2\sigma \cos\theta\left(\frac{1}{R_2} - \frac{1}{R_1}\right). \tag{B2}$$

The individual resistances for each tube, $\mathcal{R}_1$ and $\mathcal{R}_2$, are defined as:

$$\mathcal{R}_1 \coloneqq \frac{8\mu h_1}{\pi R_1^4}, \quad \mathcal{R}_2 \coloneqq \frac{8\mu h_2}{\pi R_2^4}, \tag{B3}$$

The total resistance $\mathcal{R}_{\text{total}}$ is given by the sum of the individual resistances:

$$\mathcal{R}_{\text{total}} \coloneqq \mathcal{R}_1 + \mathcal{R}_2. \tag{B4}$$

The change in height $h_i(t)$ of each tube i is influenced by both evaporation rate, $\mathcal{J}\ \left[\text{kg s}^{-1}\ \text{m}^{-2}\right]$, and capillary-induced flow rate, Q $\left[\text{m}^3\text{s}^{-1}\right]$, which can be expressed as:

$$\frac{dh_i(t)}{dt} = -\frac{\mathcal{J}}{\rho} \pm \frac{Q(t)}{A_i}. \tag{B5}$$

By taking the difference between the two height rates, we derive the equation for $\Delta h(t)$ as:

$$\frac{d\Delta h(t)}{dt} = -Q(t)\left(\frac{1}{A_1} + \frac{1}{A_2}\right). \tag{B6}$$

The final dimensional form of the governing differential equation for the height difference $\Delta h(t)$ is given by:

$$\frac{d}{dt}\Delta h(t) = \frac{\rho \pi R_1 R_2\ \left(R_1^2 + R_2^2\right)^2 (\rho g\ \Delta h(t)\ R_1 R_2 + 2\sigma \cos(\theta)(R_1 - R_2))}{8\mu\left(\pi\rho\left(R_1^6 - R_2^6\right)\Delta h(t)\ +\ \left(R_1^4 + R_2^4\right)\left(\mathcal{J}\pi R_1^2 t + \mathcal{J}\pi R_2^2 t - V_0\rho\right)\right)}. \tag{B7}$$

This equation is subject to $\left(\mathcal{J}\pi R_1^2 t\ +\ \mathcal{J}\pi R_2^2 t\ -\ V_0\rho\right) < 0$ to ensure the evaporated mass cannot be larger than the initial mass. Equation B7 can be written in the nondimensional form, as follows.

$$\frac{d\xi}{d\tilde{t}} = \frac{\lambda\pi\left(1 + \lambda^2\right)^2 (\text{Bo}\ \xi\lambda + 2 - 2\lambda)}{8\left[\pi\xi\left(1 - \lambda^6\right) + \left(1 + \lambda^4\right)\left(\tilde{\mathcal{J}}\left(1 + \lambda^2\right) - \tilde{V}_0\right)\right]}, \tilde{\mathcal{J}}\left(1 + \lambda^2\right) - \tilde{V}_0 < 0 \tag{B8}$$

where the following nondimensional numbers have been used:

$$\xi = \frac{\Delta h}{R_1}, \quad T_c = \frac{\mu R_1}{\sigma \cos\theta}, \quad \tilde{t} = \frac{t}{T_c}, \quad \lambda = \frac{R_2}{R_1}, \quad Bo = \frac{\rho g R_1^2}{\sigma \cos\theta}, \quad \tilde{\mathcal{J}} = \frac{J\pi t}{\rho R_1}, \quad \tilde{V}_0 = \frac{V_0}{R_1^3}. \tag{B9}$$

ξ is the nondimensional height difference, T_c denotes the visco-capillary characteristic timescale $\tilde{t}$ denotes the nondimensional time, λ represents the nondimensional radius ratio, Bo is the Bond number, representing the ratio of gravitational to capillary forces. A larger Bond number indicates that gravitational forces are dominant, while a smaller value suggests that capillary forces are more significant, $\tilde{\mathcal{J}}$ is the nondimensional evaporation rate, and finally $\tilde{V}_0$ represents the nondimensional initial volume.

Equation B9 captures the evolution of the height difference ξ as a function of nondimensional time $\tilde{t}$, Bond number Bo, and the nondimensional radius ratio λ. To find the steady-state solution of the nondimensional governing equation, we set $\frac{d\xi}{d\tilde{t}} = 0$, representing the condition where the height difference ξ no longer changes with time, indicating no mass exchange between the capillary tube while still evaporation is active. Substituting this into our nondimensional equation and simplifying, we obtain:

$$\Delta H_{\text{eq}} = \frac{2(\lambda - 1)}{Bo\ \lambda}, \tag{B10}$$

where ΔH_{eq} represents the equilibrium height difference in nondimensional terms. Reverting to dimensional form, the equilibrium height difference ΔH_{eq}, as proposed by Jurin's law is resulted (White, 1990):

$$\Delta H_{\text{eq}} = \frac{2\sigma \cos\theta}{\rho g}\left(\frac{1}{R_1} - \frac{1}{R_2}\right). \tag{B11}$$

When the initial nondimensional height difference is set to zero ($\xi(0) = 0$), both tubes have the same liquid level. Under this condition, ξ increases over time, approaching the equilibrium value ξ_{eq} determined by the balance of capillary, evaporation, and hydrostatic pressures. This increase is driven by the capillary pressure difference due to the differing radii of the tubes and evaporation rate.

As λ increases, the equilibrium height difference ξ_{eq} increases in magnitude. A larger λ corresponds to a greater difference between the radii of the two tubes, enhancing the capillary pressure difference driving the flow. Consequently, the system takes a longer time to reach equilibrium (see Figures B1a and B1c). The increased time to reach equilibrium is due to the higher flow resistance associated with the larger difference in tube diameters, which slows down the rate at which the liquid levels adjust to the equilibrium state.

Increasing Bo decreases the magnitude of the equilibrium height difference ξ_{eq}. Physically, a higher Bo signifies stronger gravitational forces relative to capillary forces. As a result, the capillary-induced height difference between the tubes is reduced. Additionally, a larger Bo results in a faster approach to equilibrium-the nondimensional time $\tilde{t}$ required for ξ to reach ξ_{eq} decreases with increasing Bo (see Figures B1b and B1d). This behavior occurs because stronger gravitational forces accelerate the redistribution of liquid between the tubes to balance the hydrostatic pressure difference.

Appendix C: Grid Convergence Analysis: Capillary Rise With Evaporation

Figure C1 shows the relative errors of the height difference ΔH versus grid spacing h on log–log axes (with $\Delta x = \Delta y = h$), for both L_2 and L_∞. Errors decrease monotonically under uniform refinement, and a least-squares fit of $\log(\text{error}) = a + p \log h$ gives an observed order of $p \simeq 0.90$ (L_2) and $p \simeq 0.96$ (L_∞), consistent with first-order behavior near interfaces.

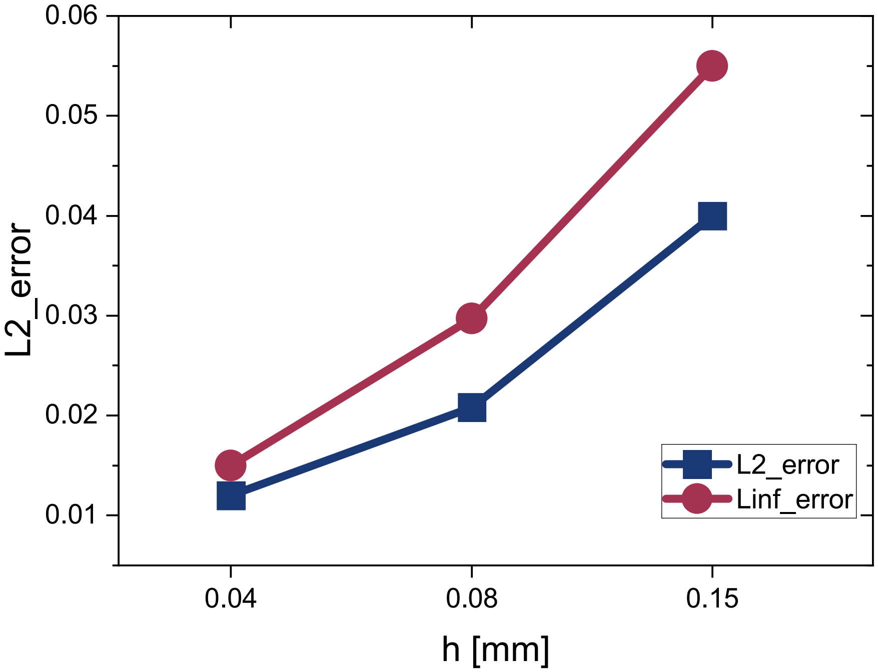

Figure C1. Grid convergence for capillary rise with evaporation: relative error of ΔH versus grid spacing h (log–log). Both L_2 and L_∞ norms are shown; fitted slopes give $p \approx 0.9$–1.0.

Conflict of Interest

The authors declare no conflicts of interest relevant to this study.

Data Availability Statement

Simulation data used in this study, including time-resolved velocity, pressure, and phase distributions for both 2D and 3D cases, are openly available on Zenodo (Mohammadrezaei et al., 2025): https://doi.org/10.5281/zenodo.15228442. These include 'vti' files for all simulation outputs, as well as the processed Excel data used for the generation and analysis of figures.

The underlying Lattice-Boltzmann code is described in full within the manuscript, and the provided data set is sufficient to reproduce the results. Figures were created using MATLAB R2023b and Origin 2024. All input data, outputs, and scripts used for plotting figures are included in the Zenodo archive.

Acknowledgments
This PhD project is funded by Shell Global Solutions International BV within the Pore-scale study of hydrate and Salt formation during CO_2 injection (HYSA) Project. VN's time, as the PI, is funded by EPSRC EP/W008718/1 Performance and Injectivity of CO_2 in Hyper-Saline Aquifers project. The authors thank Paria Beygi for designing the cover art and assisting with data visualisation.

References

Alpak, F., Berg, S., & Zacharoudiou, I. (2018). Prediction of fluid topology and relative permeability in imbibition in sandstone rock by direct numerical simulation. *Advances in Water Resources*, *122*, 49–59. https://doi.org/10.1016/j.advwatres.2018.09.001

An, S., Erfani, H., Hellevang, H., & Niasar, V. (2021). Lattice-Boltzmann simulation of dissolution of carbonate rock during CO_2-saturated brine injection. *Chemical Engineering Journal*, *408*, 127235. https://doi.org/10.1016/j.cej.2020.127235

An, S., Zhan, Y., Mahani, H., & Niasar, V. (2022). Kinetics of wettability alteration and droplet detachment from a solid surface by low-salinity: A lattice-Boltzmann method. *Fuel*, *329*, 125294. https://doi.org/10.1016/j.fuel.2022.125294

Baumann, G., Henninges, J., & De Lucia, M. (2014). Monitoring of saturation changes and salt precipitation during CO_2 injection using pulsed neutron-gamma logging at the Ketzin pilot site. *International Journal of Greenhouse Gas Control*, *28*, 134–146. https://doi.org/10.1016/j.ijggc.2014.06.023

Bette, S., & Heinemann, R. (1989). Compositional modeling of high-temperature gas-condensate reservoirs with water vaporization. In *SPE Reservoir Simulation Conference?* (p. SPE-18422).

Boltzmann, L. (1964). In S. G. Brush (Eds.), *Lectures on gas theory*. University of California Press. (UC Press reissued 2022).

Chauvet, F., Duru, P., Geoffroy, S., & Prat, M. (2009). Three periods of drying of a single square capillary tube. *Physical Review Letters*, *103*(12), 124502. https://doi.org/10.1103/physrevlett.103.124502

De Rosis, A., & Coreixas, C. (2020). Multiphysics flow simulations using d3q19 lattice Boltzmann methods based on central moments. *Physics of Fluids*, *32*(11), 117101. https://doi.org/10.1063/5.0026316

Durst, F. (2008). *Fluid mechanics: An introduction to the theory of fluid flows*. Springer.

Fei, L., Qin, F., Zhao, J., Derome, D., & Carmeliet, J. (2022). Pore-scale study on convective drying of porous media. *Langmuir*, *38*(19), 6023–6035. https://doi.org/10.1021/acs.langmuir.2c00267

Fei, L., Qin, F., Zhao, J., Derome, D., & Carmeliet, J. (2023). Lattice Boltzmann modelling of isothermal two-component evaporation in porous media. *Journal of Fluid Mechanics*, *955*, A18. https://doi.org/10.1017/jfm.2022.1048

Frank, F., Liu, C., Alpak, F. O., Berg, S., & Riviere, B. (2018). Direct numerical simulation of flow on pore-scale images using the phase-field method. *SPE Journal*, *23*(5), 1833–1850. https://doi.org/10.2118/182607-pa

Georgiadis, A., Maitland, G., Trusler, J. M., & Bismarck, A. (2010). Interfacial tension measurements of the (H_2O+ CO_2) system at elevated pressures and temperatures. *Journal of Chemical & Engineering Data*, *55*(10), 4168–4175. https://doi.org/10.1021/je100198g

Godts, S., Orr, S. A., Desarnaud, J., Steiger, M., Wilhelm, K., De Clercq, H., et al. (2021). Nacl-related weathering of stone: The importance of kinetics and salt mixtures in environmental risk assessment. *Heritage Science*, *9*(1), 1–13. https://doi.org/10.1186/s40494-021-00514-3

Gunstensen, A. K., Rothman, D. H., Zaleski, S., & Zanetti, G. (1991). Lattice Boltzmann model of immiscible fluids. *Physical Review A*, *43*(8), 4320–4327. https://doi.org/10.1103/physreva.43.4320

Haruzi, P., Katsman, R., Halisch, M., Waldmann, N. D., & Spiro, B. (2019). Petrophysical measurements of sandstone samples extracted from an outcrop [Dataset]. *PANGAEA*. https://doi.org/10.1594/PANGAEA.907552

IPCC. (2022). Summary for policymakers [Book Section]. In P. R. Shukla, J. Skea, R. Slade, A. Al Khourdajie, R. van Diemen, D. McCollum, et al. (Eds.), *Climate change 2022: Mitigation of climate change. Contribution of working group III to the sixth assessment report of the intergovernmental panel on climate change*. Cambridge University Press. https://doi.org/10.1017/9781009157926.001

Jasinski, R., Sablerolle, W., & Amory, M. (1997). Etap: Scale prediction and contol for the heron cluster. In *SPE Annual Technical Conference and exhibition?* (p. SPE-38767). https://doi.org/10.2118/38767-MS

Joekar-Niasar, V., & Hassanizadeh, S. (2012). Analysis of fundamentals of two-phase flow in porous media using dynamic pore-network models: A review. *Critical Reviews in Environmental Science and Technology*, *42*(18), 1895–1976. https://doi.org/10.1080/10643389.2011.574101

Kim, J., & Lowengrub, J. (2005). Phase field modeling and simulation of three-phase flows. *Interfaces and Free Boundaries*, *7*(4), 435–466. https://doi.org/10.4171/ifb/132

Körner, C., Thies, M., Hofmann, T., Thürey, N., & Rüde, U. (2005). Lattice Boltzmann model for free surface flow for modeling foaming. *Journal of Statistical Physics*, *121*, 179–196.

Latt, J., Malaspinas, O., Kontaxakis, D., Parmigiani, A., Lagrava, D., Brogi, F., et al. (2021). Palabos: Parallel lattice Boltzmann solver. *Computers & Mathematics with Applications*, *81*, 334–350. (Development and Application of Open-source Software for Problems with Numerical PDEs). https://doi.org/10.1016/j.camwa.2020.03.022

Lehmann, P., Assouline, S., & Or, D. (2008). Characteristic lengths affecting evaporative drying of porous media. *Physical Review E: Statistical, Nonlinear, and Soft Matter Physics*, *77*(5), 056309. https://doi.org/10.1103/physreve.77.056309

Lehmann, P., & Or, D. (2009). Evaporation and capillary coupling across vertical textural contrasts in porous media. *Physical Review E: Statistical, Nonlinear, and Soft Matter Physics*, *80*(4), 046318. https://doi.org/10.1103/physreve.80.046318

Lemmon, E. W., Huber, M. L., & McLinden, M. O. (2010). NIST standard reference database 23. In *Reference fluid thermodynamic and transport properties (REFPROP), version, 9*.

Liu, H., Kang, Q., Leonardi, C. R., Schmieschek, S., Narváez, A., Jones, B. D., et al. (2016). Multiphase lattice Boltzmann simulations for porous media applications: A review. *Computational Geosciences*, *20*(4), 777–805. https://doi.org/10.1007/s10596-015-9542-3

Mohammadrezaei, S., Niasar, V., & Farajzadeh, R. (2025). Dataset for modelling the drying process of CO_2-water in porous media with a novel volume-of-fluid lattice Boltzmann model [Dataset]. *Zenodo Repository*. https://doi.org/10.5281/zenodo.15228442

Mohammadrezaei, S., Siavashi, M., & Asiaei, S. (2022). Surface topography effects on dynamic behavior of water droplet over a micro-structured surface using an improved-vof based lattice Boltzmann method. *Journal of Molecular Liquids*, *350*, 118509. https://doi.org/10.1016/j.molliq.2022.118509

Norouzi, A. M., Babaei, M., Han, W. S., Kim, K.-Y., & Niasar, V. (2021). CO_2-plume geothermal processes: A parametric study of salt precipitation influenced by capillary-driven backflow. *Chemical Engineering Journal*, *425*, 130031. https://doi.org/10.1016/j.cej.2021.130031

Or, D., Lehmann, P., Shahraeeni, E., & Shokri, N. (2013). Advances in soil evaporation Physics—A review. *Vadose Zone Journal*, *12*(4), 1–16. https://doi.org/10.2136/vzj2012.0163

Ott, H., Andrew, M., Snippe, J., & Blunt, M. J. (2014). Microscale solute transport and precipitation in complex rock during drying. *Geophysical Research Letters*, *41*(23), 8369–8376. https://doi.org/10.1002/2014gl062266

Ott, H., Roels, S., & De Kloe, K. (2015). Salt precipitation due to supercritical gas injection: I. Capillary-driven flow in unimodal sandstone. *International Journal of Greenhouse Gas Control*, *43*, 247–255. https://doi.org/10.1016/j.ijggc.2015.01.005

Ott, H., Snippe, J., & de Kloe, K. (2021). Salt precipitation due to supercritical gas injection: II. Capillary transport in multi porosity rocks. *International Journal of Greenhouse Gas Control*, *105*, 103233. https://doi.org/10.1016/j.ijggc.2020.103233

Page, B., Turan, G., Zapantis, A., Burrows, J., Consoli, C., Erikson, J., et al. (2020). *The global status of ccs 2020: Vital to achieve net zero*. (Tech. Rep.). Global CCS Institute.

Panda, D., Supriya, B., Kharaghani, A., Tsotsas, E., & Surasani, V. K. (2020). Lattice Boltzmann simulations for micro-macro interactions during isothermal drying of bundle of capillaries. *Chemical Engineering Science*, *220*, 115634. https://doi.org/10.1016/j.ces.2020.115634

Peysson, Y., André, L., & Azaroual, M. (2014). Well injectivity during CO_2 storage operations in deep saline Aquifers—Part 1: Experimental investigation of drying effects, salt precipitation and capillary forces. *International Journal of Greenhouse Gas Control*, *22*, 291–300. https://doi.org/10.1016/j.ijggc.2013.10.031

Prawiranto, K., Defraeye, T., Derome, D., Bühlmann, A., Hartmann, S., Verboven, P., et al. (2019). Impact of drying methods on the changes of fruit microstructure unveiled by x-ray micro-computed tomography. *RSC Advances*, *9*(19), 10606–10624. https://doi.org/10.1039/C9RA00648F

Pruess, K., & Müller, N. (2009). Formation dry-out from CO_2 injection into saline aquifers: 1. Effects of solids precipitation and their mitigation. *Water Resources Research*, *45*(3). https://doi.org/10.1029/2008WR007101

Qazi, M. J., Bonn, D., & Shahidzadeh, N. (2019). Drying of salt solutions from porous media: Effect of surfactants. *Transport in Porous Media*, *128*(3), 881–894. https://doi.org/10.1007/s11242-018-1164-5

Shan, X., & Chen, H. (1993). Lattice Boltzmann model for simulating flows with multiple phases and components. *Physical Review*, *47*(3), 1815–1819. https://doi.org/10.1103/physreve.47.1815

Shan, X., & Chen, H. (1994). Simulation of nonideal gases and liquid-gas phase transitions by the lattice Boltzmann equation. *Physical Review E*, *49*(4), 2941–2948. https://doi.org/10.1103/physreve.49.2941

Skjaeveland, S., Siqveland, L., Kjosavik, A., Thomas, W., & Virnovsky, G. (2000). Capillary pressure correlation for mixed-wet reservoirs. *SPE Reservoir Evaluation and Engineering*, *3*(1), 60–67. https://doi.org/10.2118/60900-pa

Sokama-Neuyam, Y. A., Yusof, M. A. M., Owusu, S. K., Darkwah-Owusu, V., Turkson, J. N., Otchere, A. S., & Ursin, J. R. (2023). Experimental and theoretical investigation of the mechanisms of drying during CO_2 injection into saline reservoirs. *Scientific Reports*, *13*(1), 9155. https://doi.org/10.1038/s41598-023-36419-3

Sourya, D. P., Panda, D., Kharaghani, A., Tsotsas, E., Gurugubelli, P. S., & Surasani, V. K. (2023). Lattice Boltzmann simulations for the drying of porous media with gas–side convection–diffusion boundary. *Physics of Fluids*, *35*(11), 113324. https://doi.org/10.1063/5.0171573

Spycher, N., Pruess, K., & Ennis-King, J. (2003). CO_2-H_2O mixtures in the geological sequestration of CO_2. I. Assessment and calculation of mutual solubilities from 12 to 100 c and up to 600 bar. *Geochimica et Cosmochimica Acta*, *67*(16), 3015–3031. https://doi.org/10.1016/s0016-7037(03)00273-4

Sukop, M. C., & Or, D. (2004). Lattice Boltzmann method for modeling liquid-vapor interface configurations in porous media. *Water Resources Research*, *40*(1). https://doi.org/10.1029/2003WR002333

Swift, M. R., Orlandini, E., Osborn, W., & Yeomans, J. (1996). Lattice Boltzmann simulations of liquid-gas and binary fluid systems. *Physical Review E*, *54*(5), 5041–5052. https://doi.org/10.1103/physreve.54.5041

Swift, M. R., Osborn, W., & Yeomans, J. (1995). Lattice Boltzmann simulation of nonideal fluids. *Physical Review Letters*, *75*(5), 830–833. https://doi.org/10.1103/physrevlett.75.830

Thorimbert, Y., Lätt, J., & Chopard, B. (2019). Coupling of lattice Boltzmann shallow water model with lattice Boltzmann free-surface model. *Journal of Computational Science*, *33*, 1–10. https://doi.org/10.1016/j.jocs.2019.01.006

Thürey, N., Körner, C., & Rüde, U. (2005). *Interactive free surface fluids with the lattice Boltzmann method*. Technical Report 05-4. University of Erlangen-Nuremberg.

Timm, K., Kusumaatmaja, H., Kuzmin, A., Shardt, O., Silva, G., & Viggen, E. (2016). *The lattice Boltzmann method: Principles and practice*. Springer International Publishing AG.

Wheeler, I. S., Narsimhan, V., & Alexeenko, A. A. (2024). Rarefied porous flow in lyophilization: Review and open questions. In *AIP Conference proceedings* (Vol. 2996).

White, F. M. (1990). Fluid mechanics.

Yan, L., Niftaliyev, R., Voskov, D., & Farajzadeh, R. (2025). Dynamics of salt precipitation at pore scale during CO_2 subsurface storage in saline aquifer. *Journal of Colloid and Interface Science*, *678*, 419–430. https://doi.org/10.1016/j.jcis.2024.08.265

Zachariah, G. T., Panda, D., & Surasani, V. K. (2019). Lattice Boltzmann simulations for invasion patterns during drying of capillary porous media. *Chemical Engineering Science*, *196*, 310–323. https://doi.org/10.1016/j.ces.2018.11.003